Wolf, S. G., Huismans, R. S., Braun, J., Yuan, X. (2022): Topography of mountain belts controlled by rheology and surface processes. - Nature, 606, 516-521.

https://doi.org/10.1038/s41586-022-04700-6

Topography of mountain belts controlled by rheology and surface processes

Sebastian G. Wolf[1*], Ritske S. Huismans[1], Jean Braun[2,3], Xiaoping Yuan[4,2]

[1]*Department of Earth Science,University of Bergen, Bergen, Norway*
[2]*Helmholtz Centre Potsdam, German Research Centre for Geosciences, Potsdam, Germany*
[3]*Institute of Geosciences, University of Potsdam, Potsdam, Germany*
[4]*Hubei Key Laboratory of Critical Zone Evolution, School of Earth Sciences, China University of Geosciences, Wuhan, China*

It is widely recognized that collisional mountain belt topography is generated by crustal thickening and lowered by river bedrock erosion, linking climate and tectonics[1–4]. However, whether surface processes or lithospheric strength control mountain belt height, shape and longevity remains uncertain. Additionally, how to reconcile high erosion rates in some active orogens, with long-term survival of mountain belts for 100s of million years remains enigmatic. Here we investigate mountain belt growth and decay using a new coupled surface process[5,6] and mantle-scale tectonic model[7]. End-member models and the new non-dimensional Beaumont number, Bm, quantify how surface processes and tectonics control the topographic evolution of mountain belts, and allow defining three end-member types of growing orogens: Type 1, non-steady state, strength controlled ($Bm > 0.5$); Type 2, flux steady state[8], strength controlled ($Bm \approx 0.4 - 0.5$); and Type 3, flux steady state, erosion controlled ($Bm < 0.4$). Our results indicate that tectonics dominate in Himalaya-Tibet and the Central Andes (both Type 1), efficient surface processes balance high convergence rates in Taiwan (likely Type 2), and surface processes dominate in the Southern Alps of New Zealand (Type 3). Orogenic decay is determined by erosional efficiency and can be subdivided into two phases with variable isostatic rebound characteristics and associated timescales. The results presented here provide for the first time a unified framework explaining how surface processes and lithospheric strength control the height, shape, and longevity of mountain belts.

Creation and decay of orogenic topography

Mountain belt evolution in collisional settings comprises crustal thickening and surface uplift, followed by tectonic quiescence and isostatic rebound that may include extensional collapse. Surface processes shape mountain belt surface morphology by counteracting tectonic growth and by causing topographic decay. End-member collisional mountain belt types[9] include (i) active, narrow orogens with high rock uplift and erosion rates such as Taiwan and the South-

*Corresponding Author, e-mail: sebastian.wolf@uib.no

ern Alps of New Zealand, (ii) active, wide orogens with orogenic plateaus and overall low erosion rates such as Himalaya-Tibet and the Andes, and (iii) inactive orogens with slowly decaying topography surviving tens to several hundreds of million of years such as the Urals or the Appalachians. High erosion rates in small orogens, co-existence on Earth of large and small orogens of variable height, and long-term survival of orogenic topography, raise fundamental questions on the factors controlling width, height and longevity of mountain belts during their growth and decay phases. In non-glaciated mountain belts, rainfall and river incision control erosional efficiency, denudation rate, and sediment yield[2,10,11], implying that climate may set the width, height, and relief in growing orogens[2,3,12–18]. Erosional efficiency is also thought to control the longevity of mountainous relief[19,20]. However, others have shown[21–24] that finite crustal strength may be the main factor limiting the maximum elevation of orogens under some circumstances, demonstrating the need for a proper representation of tectonic deformation to study the effect of erosional efficiency on mountain growth and decay that includes isostasy, mantle lithosphere subduction, discrete faulting, and proper earth-like rheologies.

Coupled tectonic - surface process model

We use the thermo-mechanical tectonic model FANTOM[7,25] coupled to the landscape evolution model FastScape[5,6], resolving the interaction between upper mantle scale tectonic deformation and surface processes at high resolution. FANTOM computes deformation of earth-like materials with frictional-plastic and non-linear thermally-activated viscous flow, while FastScape solves for river erosion, hillslope processes, sediment transport and deposition (Methods, Extended Data Fig. 1). Erosional efficiency depends mostly on fluvial erodibility K_f, which spans several orders of magnitude owing to its dependence on rainfall, rainfall variability, lithology, fracturation, vegetation cover, and abrasive agents[14,20,26–29]. We present three end-member models with low (Model 1), high (Model 2), and very high (Model 3) fluvial erodibility (Figs. 1, 2).

End-member model results

In all models, shortening is accommodated by one-sided subduction of the strong lower crust and lithospheric mantle, and mountain building through crustal thickening (Figs. 1, 2, Supplementary Videos). During the first 10-12 Myr all modelled orogens first grow in height and then reach a stable maximum elevation (Fig. 2a). Models 1 and 2 reach a height of 6 km and 5 km, respectively, while Model 3 is significantly lower at 1.5 km (Fig. 2a). During convergence, low-erodibility Model 1 continuously widens through formation of thick-skinned thrust sheets, which control mountain topography and strongly affect drainage patterns. Erosion and rock uplift rates are very low compared to the convergence rate ($v_c = 1$ cm/yr) and bal-

anced in the orogen centre, but slightly higher and unbalanced at the active orogen flanks. The resulting non-steady state mountain belt is characterized by rivers flowing in prominent thrust-controlled longitudinal valleys (Fig. 1a). In contrast, high erodibility Model 2 exhibits flux steady state[8] between tectonic influx and erosional outflux (uplift/erosion ratio ∼1, see Fig. 2b) and constant orogen width (∼110 km) and height, with discrete faulting continuously perturbing the orogen. The resulting mountain belt is characterized by matching high uplift and erosion rates, consists of more than one thrust sheet, and is cut by sub-linear transverse valleys with steady-state river profiles (Fig. 1b). Very high fluvial erodibility Model 3 reaches flux steady state earlier than Model 2, does not produce thrust sheets, and forms a crustal monocline that is exhumed at the retro shear zone of the orogen (Figs. 1c, 2b). Model 1 and 2 maximum elevation is limited by crustal strength and the crustal buoyancy force is equal to the combination of the integrated strength and overpressure in the orogen foreland leading to formation of new thrust sheets (Extended Data Fig. 2). In contrast, erosion limits orogen height in Model 3, the buoyancy force does not reach the magnitude required to form new thrust sheets.

End-member models 1-3 represent three types of growing orogens with defining characteristics (Fig. 4): Type 1, non steady state, strength limited; Type 2, flux steady state, strength limited; Type 3, flux steady state, erosion limited. The sensitivity to variation in fluvial erodibility, crustal strength, and decoupling between thin-and thick-skinned deformation during orogenic growth shows that a) increasing fluvial erodibility in Type 1 orogens decreases the widening rate but not orogen height (Fig. 4b, Extended Data Figs. 3a-c, 4); b) Type 2 orogens have similar height as Type 1 and their width depends on fluvial erodibility (Fig. 4c, Extended Data Figs. 3d-f, 4); c) Type 3 orogens have similar narrow width, termed W_{min}, and their height depends on fluvial erodibility (Fig. 4d, Extended Data Figs. 3g-i, 4); d) lower crustal strength promotes lower height and greater width in strength-limited Type 1 and 2 orogens, but does not significantly affect erosion-limited Type 3 orogens (Extended Data Fig. 5); e) decoupling between thin-and thick-skinned deformation leads to similar evolution of topography but significantly different structural style in Type 1 orogens (Extended Data Fig. 6).

Decay of orogenic topography follows two phases with contrasting characteristics (see supplement for derivation of scaling laws). Short decay Phase 1 quickly removes short-wavelength fault-controlled topography of Model 1, and narrow orogenic topography of Models 2 and 3 (Fig. 1d-f), and is associated with regional isostatic rebound. Decay Phase 2 is characterised by removal of long-wavelength topography, and uplift and erosion rates (Fig. 1g-i) controlled by local isostatic rebound with a ratio of the average crustal and lithospheric densities (0.86, Fig. 2b). Phase 2 orogenic decay timescale is controlled by erosional efficiency, ratio of crust and lithospheric mantle density, and width and initial height of the orogen (Extended Data Fig. 7). A simple scaling law explains why Model 1 retains maximum topography of ∼1500 m even after 150 Myr of decay, while Models 2 and 3 loose all orogenic topography after few tens of Myr of decay (Fig. 2, Extended Data Fig. 7). Note that loss of topography through extensional collapse corresponds to a shift in time on the decay curve

(Extended Data Fig. 7h).

Quantifying orogenesis: the Beaumont number

Our model results show that crustal strength and surface process efficiency determine the topographic evolution of growing Type 1-3 orogens. We define the new non-dimensional Beaumont-number, Bm, as the ratio of two well established non-dimensional numbers relating tectonics and surface processes (Extended Data Fig. 8). For growing collisional orogens Bm is given as the ratio between: 1) The Argand number[31], Ar, relating the buoyancy force associated with orogenic crustal thickening to the resistance of orogenic foreland crust to deformation and orogen widening, and 2) the surface processes Damköhler number determining surface processes efficiency (Extended Data Fig. 8). Fluvial erosion is dominant in non-glaciated mountain belts, and $Da_{SP}IV$, corresponding to the uplift-erosion number N_e[2,10], determines relative importance of erosional power and surface uplift, so that

$$Bm = \frac{Ar}{N_e} \propto \frac{v_c}{F_{int} K_f} \,. \tag{1}$$

Bm provides a simple and unique description of the factors controlling orogenic growth, relating convergence velocity (v_c), crustal strength (F_{int}), surface processes efficiency (K_f), and other more easily measurable parameters (e.g., crustal thickness, see derivation in supplement). Models with variable fluvial erodibility, plate velocity, and crustal strength show systematic variation of Bm, with all models fitting on a single curve (Fig. 3a): Strength-limited non steady state Type 1 orogens (Fig. 4b) have $Bm > 0.5$, strength-limited flux steady state Type 2 orogens (Fig. 4c) have $Bm \approx 0.4 - 0.5$, while erosion-limited flux steady state Type 3 orogens (Fig. 4d) have $Bm < 0.4$. In turn, knowing Bm of active orogens allows approximating crustal strength and average fluvial erodibility, two highly unknown values.

The Beaumont number of active orogens

The Southern Alps of New Zealand (SANZ), Taiwan, Himalaya-Tibet, and the Central Andes (see supplement for extensive comparison) represent the full range of orogen-types presented here. Computation of Bm and orogen type classification only requires knowledge of orogen height, width, first-order shortening distribution, crustal shortening rate, and an estimate of the fraction of eroded crustal material. We also define the longitudinality index (LI, Methods), a simple metric of river diversion into longitudinal valleys and fluvial drainage network topology complementing Bm. Modelled Type 1 orogens show non steady state river networks dominated by longitudinal valleys with $LI \approx [1.5 - 4.5]$, while Type 2 and 3

orogens have steady state river networks dominated by transverse valleys with $LI \approx [1.0-1.3]$ (Extended Data Fig. 9).

The SANZ is a type-example of an erosion-limited Type 3 orogen[2,12] and has $Bm = [0.15 - 0.48]$ (Fig. 3a,b, Extended Data Fig. 10a). Its central part forms by collision of the Pacific and Australian plates at $v_c \approx 1\,\mathrm{cm/yr}$, is about 80 km wide, exhibits extremely high exhumation rates, and is shaped primarily by transverse valleys with median $LI = 1.4$[32–35]. It resembles a crustal monocline with crustal shortening largely accommodated by thrusting on the Alpine fault and minor thrust motion in its hanging wall[33,36]. Fluvial erodibility is high and crustal strength can be confined to a range typically observed on Earth (Fig. 3b).

We propose here that Central Taiwan matches the primary characteristics of a flux steady state but strength-limited Type 2 orogen with $Bm \approx 0.4$ (Fig. 3a,c, Extended Data Fig. 10b): 1) It has a constant orogen width of 80 to 100 km in the centre, 2) a non-monoclinal orogen structure with active thrusting on both orogen flanks, 3) exhibits very high shortening and erosion rates[11], and 4) has primarily transverse valleys ($LI = 1.6$)[37–41]. Its maximum mean height of 2.8 km implies a low crustal strength of $F_{int} = 1.1 \times 10^{12}\,\mathrm{N/m}$, consistent with the weak passive margin that constitutes the mountain belt foreland[38,39,41]. Flux steady state in Taiwan requires extremely high $K_f \approx 47 \times 10^{-5}\,\mathrm{m^{0.2}/yr}$, as plate convergence is very high (Fig. 3c, Extended Data Fig. 10b).

Himalaya-Tibet is a type-example of a strength-limited Type 1 orogen with $Bm = 1.5 \pm 0.5$ (Fig. 3a,d, Extended Data Fig. 10c) with consistent characteristics: 1) a wide growing orogen with a central plateau, 2) maximum mean height of ∼5 km, 3) high average convergence rate ($v_c \approx 7\,\mathrm{cm/yr}$), and 4) longitudinal fluvial topology with $LI = 2.8$[42–44]. Bm allows estimating average fluvial erodibility $K_f = [4.7 - 12.5] \times 10^{-5}\,\mathrm{m^{0.2}/yr}$ and integrated strength $F_{int} = 2.7 \pm 0.4 \times 10^{12}\,\mathrm{N/m}$ (Fig. 3) agreeing with model values and independent estimates[45]. High average fluvial erodibility implies extremely high erosion rates in the wet frontal Himalayas, several magnitudes higher than in the dry mountain belt centre, consistent with exhumation data and modelling studies[4,46,47].

The Central Andes[48] have also characteristics of a strength-limited Type 1 orogen with $Bm = 3 \pm 1$ (Fig. 3a,e, Extended Data Fig. 10d): 1) It is actively shortening and widening ($v_c \approx 1\,\mathrm{cm/yr}$)[49], 2) exhibits a common maximum mean elevation of $\sim 4.4\,\mathrm{km}$ despite highly variable mountain width along strike, and 3) has a prominent longitudinal fluvial network with median $LI = 2.1$. Similar height but variable width of the Andes along strike is consistent with initial growth in height and then in width, and can be explained either by an along-strike change in erodibility and climate, or by variations in amount of crustal shortening[49].

We briefly summarise the primary controls determining the different orogenic system: High convergence rate dominates over high fluvial erodibility in the non-steady state Type 1 Himalaya-Tibet orogen, while similar fluvial erodibility but lower convergence rate leads

to the Type 3 steady state SANZ orogen. The Type 2 Taiwan orogen is dominated by extremely high fluvial erodibility, which otherwise would likely be a Type 1 orogen given its weak foreland crust and high convergence rate. In contrast, low shortening rates in the Central Andes dominate over very low fluvial erodibility. The Bm number for the various natural systems suggests that crustal strength on Earth varies only by a factor 2-3, while plate convergence and fluvial erodibility each span a greater range and determine orogen type (Figure 3).

Channel steepness indices (k_{sn}) for modelled orogens are consistent with actively growing and decaying orogens on Earth[18,50,51] (Extended Data Fig. 9h, Methods). Modelled k_{sn} strongly suggest that rheological control on maximum topographic relief on Earth explains the observed upper limit of steepness indices on Earth.

Characteristic mountain belt evolution

We propose here that collisional orogenic topographic evolution follows four characteristic phases (Fig. 4a) that can be understood by considering the interplay of convergence velocity, crustal rheology, and surface processes efficiency. Phase I initial orogen growth occurs until the maximum elevation (h_R) that is supported by crustal strength is reached (Type 1 and Type 2) or until erosion-limited steady state is reached (Type 3). Subsequent Phase II orogen growth occurs either at steady state with constant width for high surface process efficiency (Type 2 and 3), or at non-steady state when erosion does not balance tectonic flux, resulting in orogen widening at constant maximum elevation (Type 1). The Bm number provides a measure of steady versus non-steady-state nature, and the underlying controlling factors. Decay of orogenic topography is controlled by erosional efficiency and isostatic rebound in response to erosion. Phase III exhibits fast decay and removal of short-wavelength topography. Slow and long-term decay of topography in Phase IV is controlled by surface process efficiency and local-isostatic rebound.

We conclude that the topographic evolution of collisional orogens is determined by the combination of plate velocity, crustal rheology, and surface processes efficiency. The new Beaumont number uniquely defines mountain belts as Type 1, 2, or 3, explains their underlying controls, and allows approximation of crustal strength and average fluvial erodibility. In strength limited orogens (Type 1 and 2), erosional efficiency may control mountain belt width but not height, and mountain belt elevation puts constraints on rheology of the growing orogen. In contrast, high surface process efficiency in erosion-limited Type 3 orogens determines orogen height and leads to a characteristic structural style with constant, low orogen width. Provided erosional efficiency does not change, Bm also allows predicting the timescale and rate of orogenic decay once convergence stops, as mountain belt longevity is mostly dictated by erosional efficiency. The Central Andes, for instance, are likely to survive for a long time, possibly longer than Himalaya-Tibet, while Taiwan is likely removed within

few Myrs of tectonic inactivity. The results presented here provide for the first time a unified framework for the controls of collisional mountain belts subject to the interaction between surface processes and tectonics.

References

1. Beaumont, C., Fullsack, P. & Hamilton, J. in *Thrust tectonics* 1–18 (Springer, 1992).
2. Willett, S. D. Orogeny and orography: The effects of erosion on the structure of mountain belts. *Journal of Geophysical Research-Solid Earth* **104,** 28957–28981 (1999).
3. Whipple, K. X., Kirby, E. & Brocklehurst, S. H. Geomorphic limits to climate-induced increases in topographic relief. *Nature* **401,** 39–43 (1999).
4. Beaumont, C., Jamieson, R. A., Nguyen, M. H. & Lee, B. Himalayan tectonics explained by extrusion of a low-viscosity crustal channel coupled to focused surface denudation. *Nature* **414,** 738–742 (2001).
5. Braun, J. & Willett, S. D. A very efficient O(n), implicit and parallel method to solve the stream power equation governing fluvial incision and landscape evolution. *Geomorphology* **180,** 170–179 (2013).
6. Yuan, X. P., Braun, J., Guerit, L., Rouby, D. & Cordonnier, G. A New Efficient Method to Solve the Stream Power Law Model Taking Into Account Sediment Deposition. *Journal of Geophysical Research-Earth Surface* **124,** 1346–1365 (2019).
7. Thieulot, C. FANTOM: Two- and three-dimensional numerical modelling of creeping flows for the solution of geological problems. *Physics of the Earth and Planetary Interiors* **188,** 47–68 (2011).
8. Willett, S. D. & Brandon, M. T. On steady states in mountain belts. *Geology* **30,** 175–178 (2002).
9. Beaumont, C., Nguyen, M. H., Jamieson, R. A. & Ellis, S. Crustal flow modes in large hot orogens. *Geological Society, London, Special Publications* **268,** 91–145 (2006).
10. Whipple, K. X. & Tucker, G. E. Dynamics of the stream-power river incision model: Implications for height limits of mountain ranges, landscape response timescales, and research needs. *Journal of Geophysical Research-Solid Earth* **104,** 17661–17674 (1999).
11. Dadson, S. J. *et al.* Links between erosion, runoff variability and seismicity in the Taiwan orogen. *Nature* **426,** 648–651 (2003).
12. Koons, P. O. The Topographic Evolution of Collisional Mountain Belts - a Numerical Look at the Southern Alps, New-Zealand. *American Journal of Science* **289,** 1041–1069 (1989).
13. Molnar, P. & England, P. Late Cenozoic Uplift of Mountain-Ranges and Global Climate Change - Chicken or Egg. *Nature* **346,** 29–34 (1990).

14. Tucker, G. E. & Bras, R. L. A stochastic approach to modeling the role of rainfall variability in drainage basin evolution. *Water Resources Research* **36,** 1953–1964 (2000).

15. Hartshorn, K., Hovius, N., Dade, W. B. & Slingerland, R. L. Climate-driven bedrock incision in an active mountain belt. *Science* **297,** 2036–2038 (2002).

16. Whipple, K. X. & Meade, B. J. Orogen response to changes in climatic and tectonic forcing. *Earth and Planetary Science Letters* **243,** 218–228 (2006).

17. Willett, S. D., Schlunegger, F. & Picotti, V. Messinian climate change and erosional destruction of the central European Alps. *Geology* **34,** 613–616 (2006).

18. Hilley, G. E. *et al.* Earth's topographic relief potentially limited by an upper bound on channel steepness. *Nature Geoscience* **12,** 828–+ (2019).

19. Baldwin, J. A., Whipple, K. X. & Tucker, G. E. Implications of the shear stress river incision model for the timescale of postorogenic decay of topography. *Journal of Geophysical Research-Solid Earth* **108** (2003).

20. Egholm, D. L., Knudsen, M. F. & Sandiford, M. Lifespan of mountain ranges scaled by feedbacks between landsliding and erosion by rivers. *Nature* **498,** 475–+ (2013).

21. Molnar, P. & Lyon-Caen, H. Some simple physical aspects of the support, structure, and evolution of mountain belts. *Geol. Soc. Am. Spec. Pap.* **218,** 179–207 (1988).

22. Sandiford, M. & Powell, R. Some Isostatic and Thermal Consequences of the Vertical Strain Geometry in Convergent Orogens. *Earth and Planetary Science Letters* **98,** 154–165 (1990).

23. Zhou, S. H. & Sandiford, M. On the Stability of Isostatically Compensated Mountain Belts. *Journal of Geophysical Research-Solid Earth* **97,** 14207–14221 (1992).

24. Vanderhaeghe, O., Medvedev, S., Fullsack, P., Beaumont, C. & Jamieson, R. A. Evolution of orogenic wedges and continental plateaux: insights from crustal thermal-mechanical models overlying subducting mantle lithosphere. *Geophysical Journal International* **153,** 27–51 (2003).

25. Wolf, S. G. & Huismans, R. S. Mountain Building or Backarc Extension in Ocean-Continent Subduction Systems: A Function of Backarc Lithospheric Strength and Absolute Plate Velocities. *Journal of Geophysical Research-Solid Earth* **124,** 7461–7482 (2019).

26. Whipple, K. X. Bedrock rivers and the geomorphology of active orogens. *Annual Review of Earth and Planetary Sciences* **32,** 151–185 (2004).

27. Sklar, L. S. & Dietrich, W. E. Sediment and rock strength controls on river incision into bedrock. *Geology* **29,** 1087–1090 (2001).

28. Molnar, P., Anderson, R. S. & Anderson, S. P. Tectonics, fracturing of rock, and erosion. *Journal of Geophysical Research-Earth Surface* **112** (2007).

29. Starke, J., Ehlers, T. A. & Schaller, M. Latitudinal effect of vegetation on erosion rates identified along western South America. *Science* **367,** 1358–1361 (2020).

30. Curry, M. E., van der Beek, P., Huismans, R. S., Wolf, S. G. & Muñoz, J. A. Evolving paleotopography and lithospheric flexure of the Pyrenean Orogen from 3D flexural modeling and basin analysis. *Earth and Planetary Science Letters* **515,** 26–37 (2019).

31. Ellis, S., Fullsack, P. & Beaumont, C. Oblique Convergence of the Crust Driven by Basal Forcing - Implications for Length-Scales of Deformation and Strain Partitioning in Orogens. *Geophysical Journal International* **120,** 24–44 (1995).

32. Batt, G. E. & Braun, J. The tectonic evolution of the Southern Alps, New Zealand: insights from fully thermally coupled dynamical modelling. *Geophysical Journal International* **136,** 403–420 (1999).

33. Norris, R. J. & Cooper, A. F. Late Quaternary slip rates and slip partitioning on the Alpine Fault, New Zealand. *Journal of Structural Geology* **23,** 507–520 (2001).

34. Little, T. A. Transpressive ductile flow and oblique ramping of lower crust in a two-sided orogen: Insight from quartz grain-shape fabrics near the Alpine fault, New Zealand. *Tectonics* **23** (2004).

35. Jiao, R., Herman, F. & Seward, D. Late Cenozoic exhumation model of New Zealand: Impacts from tectonics and climate. *Earth-Science Reviews* **166,** 286–298 (2017).

36. Herman, F., Cox, S. C. & Kamp, P. J. J. Low-temperature thermochronology and thermokinematic modeling of deformation, exhumation, and development of topography in the central Southern Alps, New Zealand. *Tectonics* **28** (2009).

37. Suppe, J. A retrodeformable cross section of northern Taiwan. *Proc. Geol. Soc. China* **23,** 46–55 (1980).

38. Brown, D., Alvarez-Marron, J., Schimmel, M., Wu, Y. M. & Camanni, G. The structure and kinematics of the central Taiwan mountain belt derived from geological and seismicity data. *Tectonics* **31** (2012).

39. Brown, D. *et al.* How the structural architecture of the Eurasian continental margin affects the structure, seismicity, and topography of the south central Taiwan fold-and-thrust belt. *Tectonics* **36,** 1275–1294 (2017).

40. Simoes, M. *et al.* Mountain building in Taiwan: A thermokinematic model. *Journal of Geophysical Research-Solid Earth* **112** (2007).

41. Van Avendonk, H. J. A. *et al.* Deep crustal structure of an arc-continent collision: Constraints from seismic traveltimes in central Taiwan and the Philippine Sea. *Journal of Geophysical Research-Solid Earth* **119,** 8397–8416 (2014).

42. DeCelles, P. *et al.* in *Geodynamics of a Cordilleran Orogenic System: The Central Andes of Argentina and Northern Chile* (Geological Society of America, Jan. 2015).

43. Replumaz, A., Negredo, A. M., Guillot, S., van der Beek, P. & Villasenor, A. Crustal mass budget and recycling during the India/Asia collision. *Tectonophysics* **492,** 99–107 (2010).

44. Ingalls, M., Rowley, D. B., Currie, B. & Colman, A. S. Large-scale subduction of continental crust implied by India-Asia mass-balance calculation. *Nature Geoscience* **9,** 848–853 (2016).

45. Schmalholz, S. M., Medvedev, S., Lechmann, S. M. & Podladchikov, Y. Relationship between tectonic overpressure, deviatoric stress, driving force, isostasy and gravitational potential energy. *Geophysical Journal International* **197,** 680–696 (2014).

46. Burbank, D. W. *et al.* Bedrock incision, rock uplift and threshold hillslopes in the northwestern Himalayas. *Nature* **379,** 505–510 (1996).

47. Herman, F. *et al.* Exhumation, crustal deformation, and thermal structure of the Nepal Himalaya derived from the inversion of thermochronological and thermobarometric data and modeling of the topography. *Journal of Geophysical Research-Solid Earth* **115** (2010).

48. Oncken, O. *et al.* in *The Andes. Frontiers in Earth Sciences* (eds Oncken, O. *et al.*) 3–27 (Springer, Berlin, Heidelberg, 2006).

49. Schellart, W. P., Freeman, J., Stegman, D. R., Moresi, L. & May, D. Evolution and diversity of subduction zones controlled by slab width. *Nature* **446,** 308–311 (2007).

50. Wobus, C. W., Hodges, K. V. & Whipple, K. X. Has focused denudation sustained active thrusting at the Himalayan topographic front? *Geology* **31,** 861–864 (2003).

51. Kirby, E. & Whipple, K. X. Expression of active tectonics in erosional landscapes. *Journal of Structural Geology* **44,** 54–75 (2012).

Figure captions

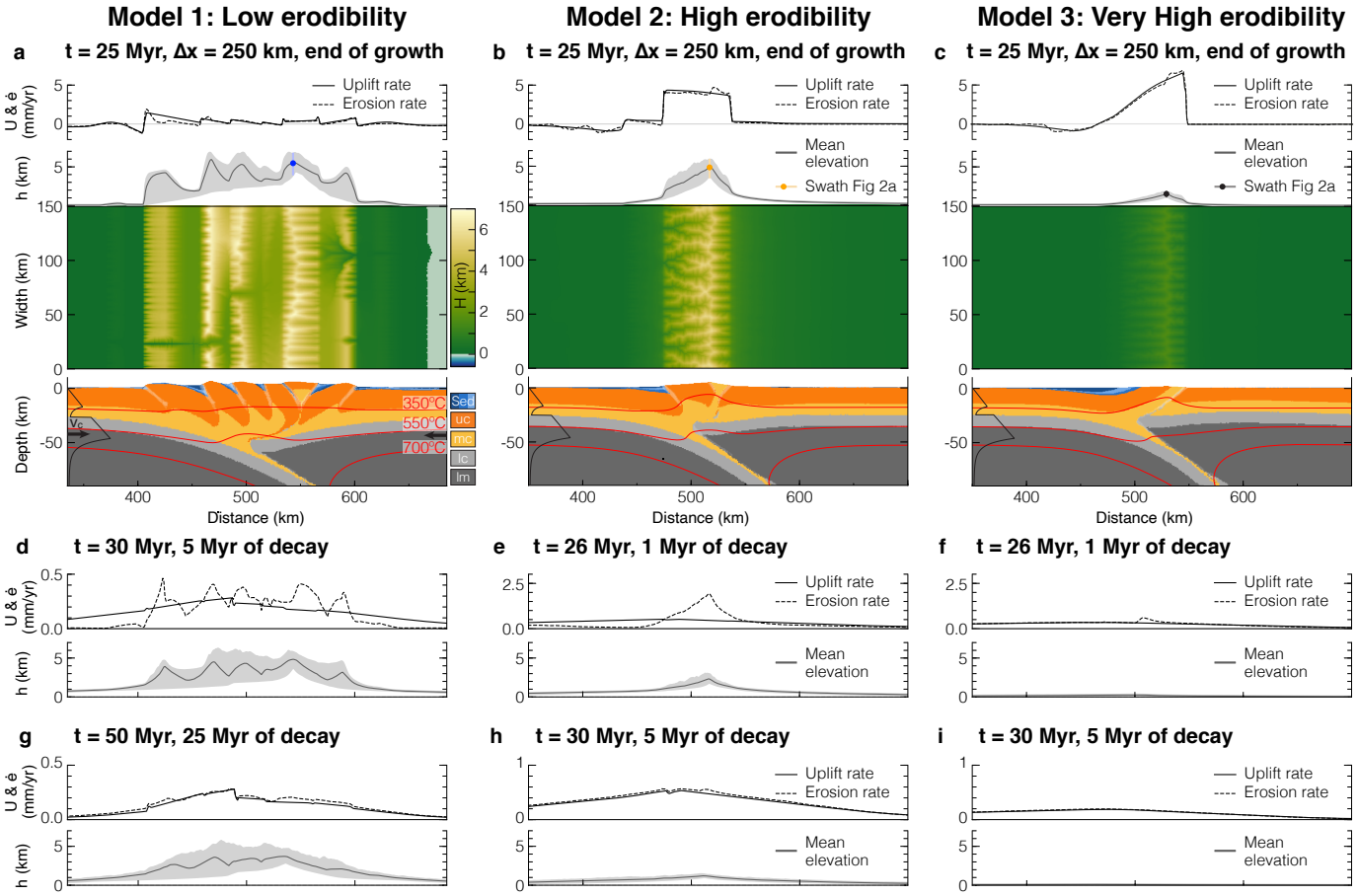

Figure 1 | Key stages for Models 1 – 3 (one model per column). a-c, Model snapshots at the end of shortening. From bottom to top: Zoom into model domain showing material distribution (sed = sediments, uc = upper crust, mc = middle crust, lc = lower crust, lm = lithospheric mantle) and temperature contours from thermo-mechanical tectonic model, map-view landscape, swath elevation profile of the landscape, and profiles of uplift (U) and average erosion rate ($\dot{e}$). t is model time, Δx is amount of convergence, v_c is convergence rate (1 cm/yr). **d-i**, Swath profile and corresponding uplift and average erosion rates during orogenic decay phase I (d-f) and phase II (g-i).

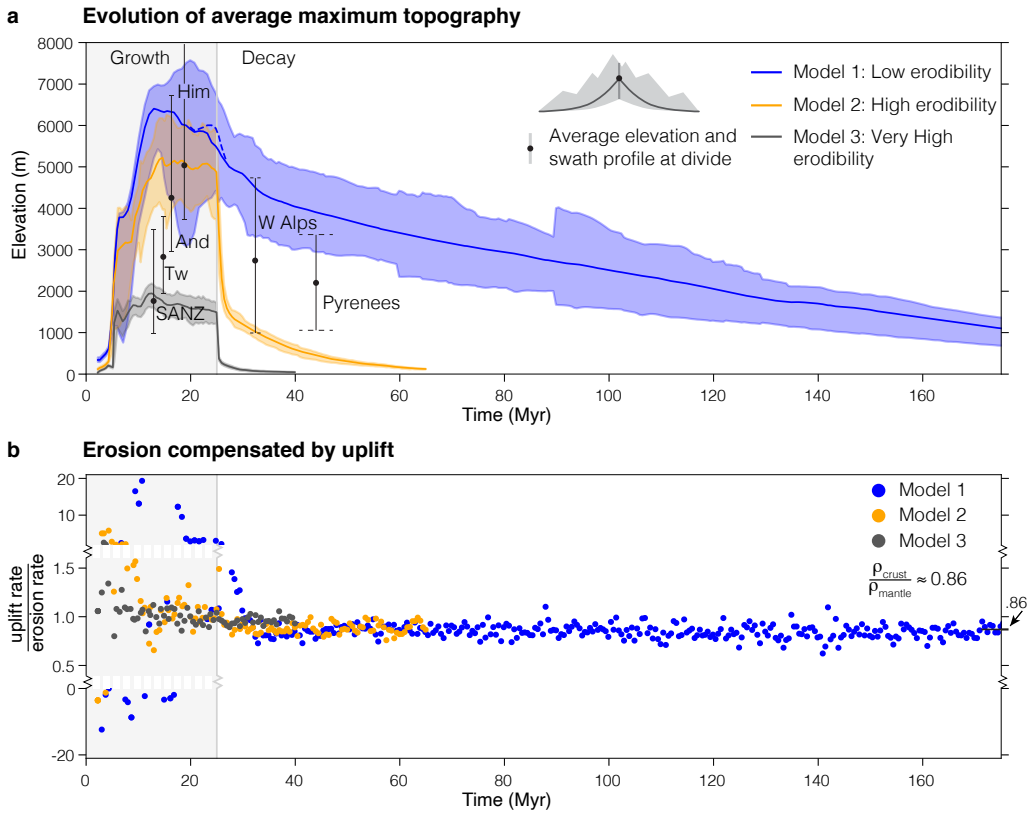

Figure 2 | Evolution of mountain belt topography. a, Evolution of the mean elevation at the main drainage divide (solid line) with corresponding shaded swath profile. The mean elevation of the main drainage divide coincides with the maximum mean elevation of the orogens. In Model 1 these measures do not coincide around 20–30 Myr, and the maximum mean elevation is additionally shown as stippled line. The grey shaded area frames the growth phase; the decay phase has a white background. Capped black bars show typical swath profiles of several orogens on Earth; dot indicates mean elevation. Swath profiles of growing orogens (And, Him, TW, SANZ, see Fig. 3) are placed with ascending height; Pyrenees and W Alps are placed according to their orogenic decay time[17,30]. Note that the swath profiles of natural systems can be explained by a combination of surface process efficiency and crustal rheology (see discussion below and in supplement). **b**, Plot showing the fraction of erosion compensated by uplift. During orogenic growth, Models 2 and 3 reach a factor close to one, showing flux steady state. In contrast, Model 1 never reaches flux steady state and has scattered values dominated by tectonic uplift and subsidence. During orogenic decay, a short phase with values greater than 1 is followed by a long phase with average values of 0.86. The latter value is close to the ratio of the density between continental crust (ρ_{crust}) and lithospheric mantle (ρ_{mantle}).

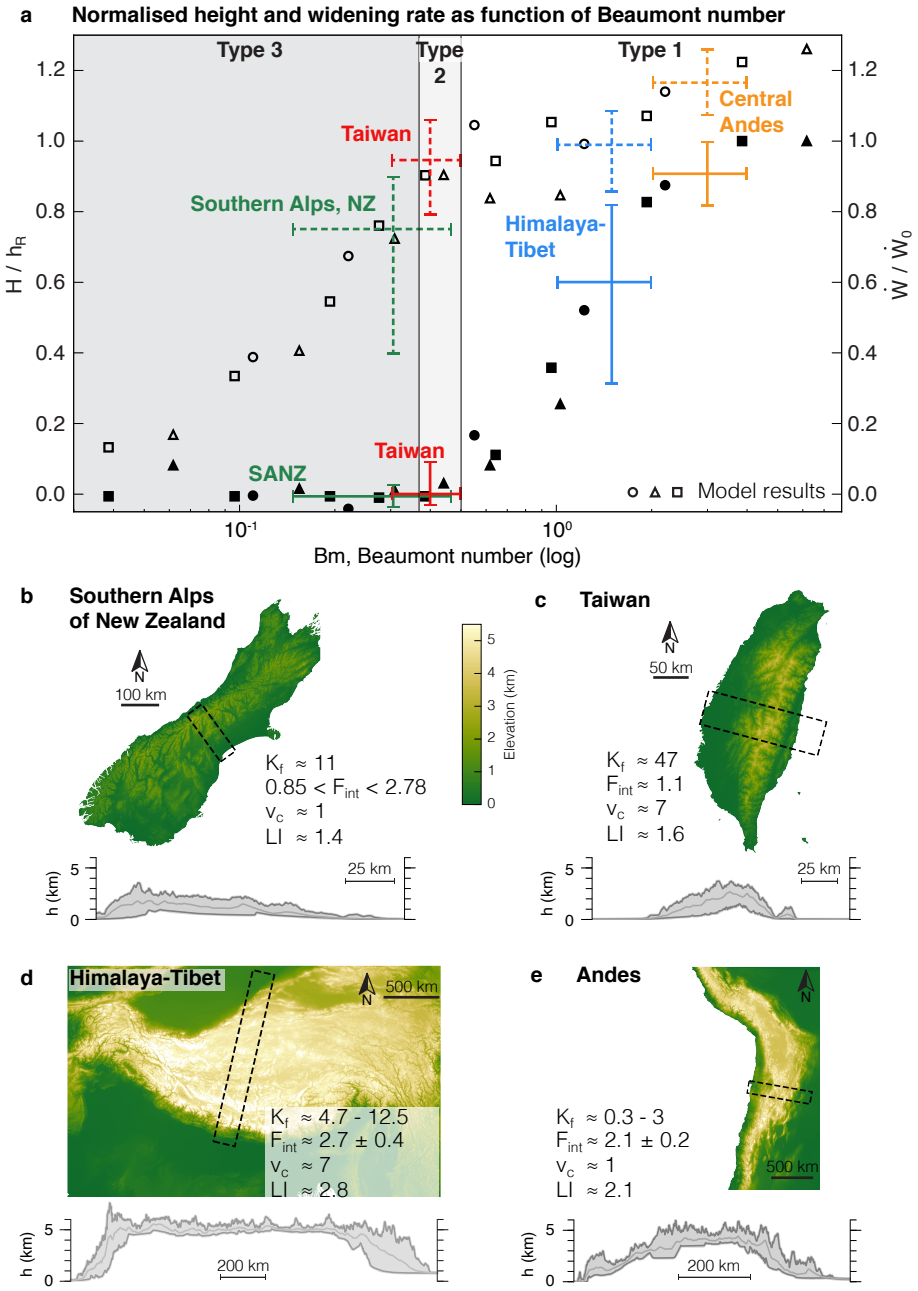

Figure 3 | Beaumont-number of models and mountain belts on Earth. a, Semilog-plot of maximum mean mountain height H normalised by the mean rheologically controlled height h_R (unfilled markers, left y-axis), and widening rate $\dot{W}$ normalised by the widening rate without surface processes $\dot{W}_0$ (filled markers, right y-axis), against Beaumont number. Squares, dots and triangles represent different model sets with variable fluvial erodibility, crustal strength, and plate velocities (model values in supplementary table 3). Large crosses show approximate positions of the Southern Alps of New Zealand, Taiwan, Himalaya-Tibet, and the Central Andes. **b-e**, DEMs and swath profiles of four orogens with computed average integrated crustal strength (F_{int} in 1×10^{12} N/m), orogen-average fluvial erodibility (K_f in $1 \times 10^{-5}\,\mathrm{m}^{0.2}/\mathrm{yr}$), average convergence velocity (v_c in cm/yr; $v_c = v_{trench} - v_{SouthAmerica}$ in the Central Andes), and longitudinality index (LI).

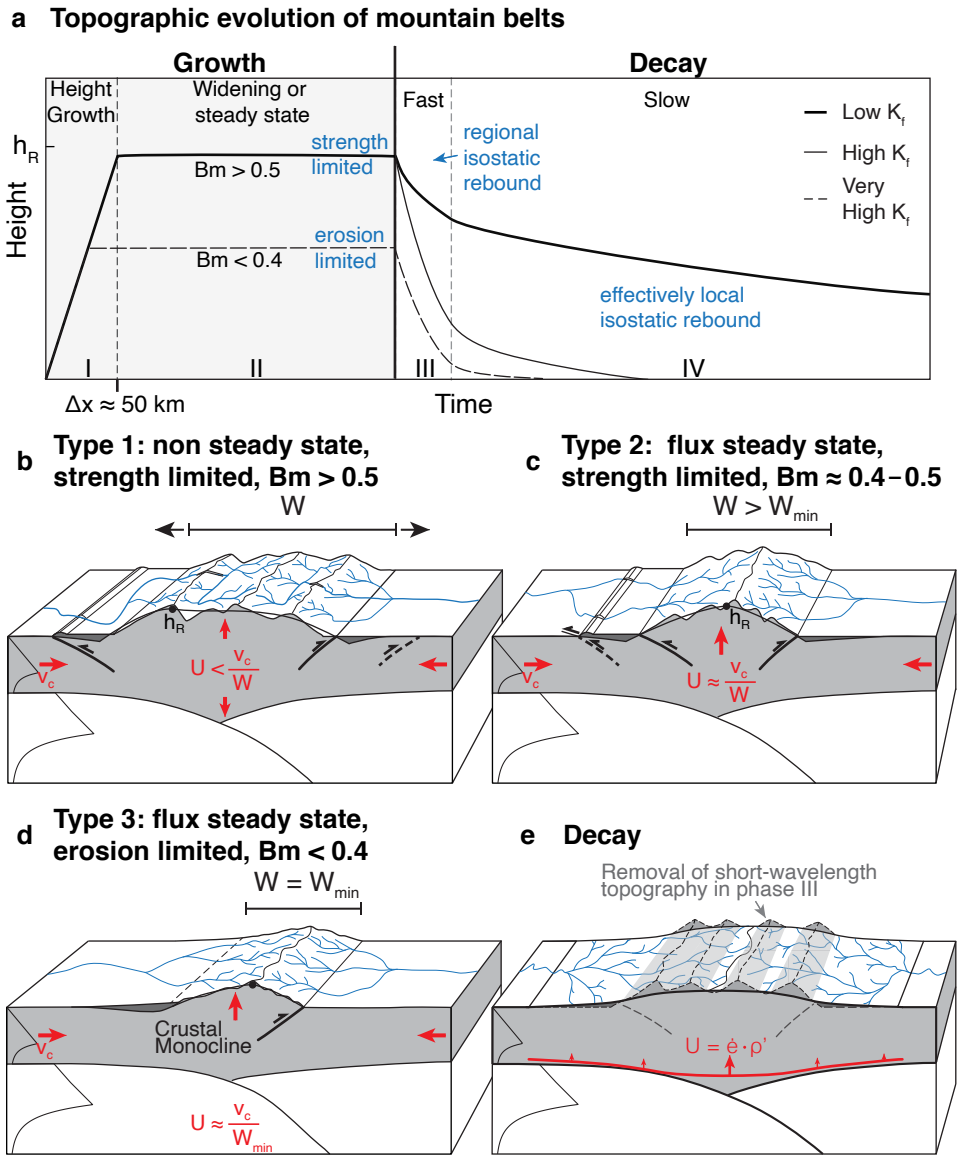

Figure 4 | Characteristic evolution of mountain belts. **a**, Simplified elevation-time diagram depicting the topographic evolution of mountain belts and its controlling factors. h_{R} is the topographic limit, which depends on crustal strength. **b-d**, Block diagrams indicating key features of Types 1, 2, 3 of growing orogens. U is uplift rate, v_c is convergence velocity, and $\dot{e}$ is erosion rate, W_{min} is the width of one crustal scale thrust sheet. **e**, Block diagram indicating key features of decaying orogens. The diagram is most representative for low K_f settings. The uplift rate is dependent on erosion rate, ratio of crust and lithospheric mantle density, and degree of regional isostatic compensation, captured in the isostatic compensation factor ρ'. Short-wavelength topography is quickly removed in phase III, before long-wavelength topography is removed slowly in phase IV.

Methods

Thermo-mechanical-landscape-evolution-model: We use the 2-dimensional Arbitrary Langrangian-Eulerian (ALE), finite element model FANTOM[7,25], computing thermo-mechanically coupled, incompressible, plane-strain, viscous-plastic creeping flows to investigate mountain building during continent-continent collision (see supplementary file). We coupled FANTOM to the 2-dimensional landscape evolution model FastScape[5,6]. FastScape directly interacts with the thermo-mechanical model, in that any deposition and erosion feeds back to the thermo-mechanical computation through its effect on gravitational stress redistribution and on rheology (see supplementary material for detailed coupling description). FastScape solves for stream power river incision (K_f-term in eq. 2), hillslope diffusion (K_d-term), sediment transport and deposition in rivers (G-term) and filling of local depressions, i.e. lakes and the mountain foreland basins:

$$\frac{\partial h}{\partial t} = U - K_f A^m S^n + K_d \nabla^2 h + \frac{G}{A}\int_A (U - \frac{\partial h}{\partial t}) dA, \tag{2}$$

where h is topographic elevation, t is time, U is uplift rate, K_f is fluvial erodibility, A is catchment area upstream, S is local slope, K_d is hillslope diffusion coefficient, G is a dimensionless deposition coefficient, and m and n are the stream power exponents. Denudational power is largely set by the efficiency of river erosion, which depends on the coefficients m, n, G, and K_f. m, n, and G are relatively well known with n ranging from $1-3$ [52], $\frac{m}{n}$ varying from $0.3-0.5$ [53], and G being in the order of 1 [54]. The fluvial erodibility K_f is characterised by large uncertainty and spans a wide range, as it incorporates variations as a function of climate, rock type, vegetation, abrasive agents and channel geometry[53]. Typical values lie between $1\times10^{-6}\,\mathrm{m}^{0.2}/\mathrm{yr}$ and $1\times10^{-4}\,\mathrm{m}^{0.2}/\mathrm{yr}$ [53], assuming $m = 0.4$ and $n = 1$. We designed three end-member models with respectively low $K_f = 0.5\times10^{-5}\,\mathrm{m}^{0.2}/\mathrm{yr}$ (Model 1), high $K_f = 5\times10^{-5}\,\mathrm{m}^{0.2}/\mathrm{yr}$ (Model 2), and very high $K_f = 20\times10^{-5}\,\mathrm{m}^{0.2}/\mathrm{yr}$ (Model 2), with $m = 0.4$, $n = 1$ and $G = 1$. The hillslope diffusion coefficient is constant with $K_d = 1\times10^{-2}\,\mathrm{m}^2/\mathrm{yr}$ [55,56]. Models are actively shortening for 25 Myr at a rate of 1 cm/yr, leading to 250 km of convergence, followed by orogenic decay without active shortening until the orogenic topography is removed by erosion.

The Beaumont number: We define the new non-dimensional Beaumont number, Bm, that captures the interaction between surface processes and tectonics. We propose the name Beaumont-number, as Beaumont *et al.* [1], and Chris Beaumont and his group during the following years, initially developed coupled tectonic-surface process models similar to ours, and used them to investigate the feedbacks between tectonics, surface processes, and ultimately climate. Bm is defined as the ratio between the essential non-dimensional number describing tectonics (N_{Tec}), and the essential non-dimensional Surface Processes Damköhler number determining surface processes efficiency (see also Extended Data Figure 8):

$$Bm = \frac{N_{Tec}}{Da_{SP}}. \tag{3}$$

For mountain belts growing by crustal thickening, one can show that the Argand number Ar of the continental crust is the key non-dimensional number describing tectonics [31, 57, 58] (see supplement for derivation). $Da_{SP}IV$ is the non-dimensional number determining mass in- and out-flux in systems dominated by fluvial surface processes, so that

$$Bm = \frac{Ar}{Da_{SP}IV} \tag{4}$$

is the Beaumont number that captures the interaction between surface processes and tectonics in actively growing collisional mountain belts. Large Bm imply inefficient surface processes, which results in Type 1 orogens, and low Bm mean that surface processes are efficiently counteracting orogenic growth, which results in Type 3 orogens.

Specifically, in case surface processes are determined by the (extended) Stream Power Law, as in our models, $Da_{SP}IV$ corresponds to the uplift-erosion number ${N_e}^{2,10}$, and

$$Bm = \frac{Ar}{N_e}. \tag{5}$$

See supplementary file for a full derivation of Bm and associated values.

Longitudinality index: We define the longitudinality index (LI) as the quotient of actual river length and shortest distance between river source and orogen boundary. To compute LI we use the modelled landscapes (Extended Data Fig. 9), and the 90-m-resolution CGIAR-SRTM v4.1 DEM of each investigated orogen (Extended Data Figs. 9c-f). The DEMs are re-scaled to 250 m (Alps, New Zealand, Taiwan) respectively 1000 m (Himalaya, Andes) resolution to ensure computational feasibility. Following Whipple *et al.* [3], we assume that any point in the landscape with a critical drainage area $A = \max(\min(A), 1 \times 10^5\,\mathrm{m}^2)$ is a source point of a river. The orogen boundaries are manually picked to align with the strike of the outermost significant orogenic topography; in our models the orogen boundaries are defined at an average model elevation of 350 m. Only rivers draining through the predefined boundaries are considered for computation. River length and long profiles are computed using the FastScape steepest-descent algorithm, with hydraulic continuity ensured by lateral connection of local minima for instance related to artefacts in the DEM. We note that our calculations create only theoretical river networks which for instance also connect endorheic basins to base-level. We consider this first order representation of fluvial networks as sufficient for our data analysis. Rivers naturally build a dendritic network with laterally flowing tributaries. To separate tributaries from river flow diverted by tectonic activity, we impose a simple minimum distance between source point and orogen boundary of 15 km. The minimum distance is reduced to 12 km in the NW flank of the Southern Alps of New Zealand, to ensure proper source point coverage in this area. We stress that points with high longitudinality indices and large distance to the orogen boundary indicate that tectonic topography is persistently not removed by surface processes. These source points are therefore more significant than source points close to the boundary, where newly forming thrusts

only transiently divert river flow. For simplicity, we did not introduce complicating factors, for instance distance-weighting, to our data points. Most notably the Southern Alps of New Zealand are characterized by many Quaternary glacial valleys. For our analysis we assume that glaciers followed the pre-existing river network, so that longitudinality indices are to first order also meaningful in theses orogens.

Steepness index: We compute the steepness index in Fig. 3d with $k_{sn} = A^{\frac{m}{n}}S$, see Wobus *et al.*[59]. Yuan *et al.*[6] showed that including sediment deposition, as utilized in our model simulations (Fig. 2), increases the steepness index at steady state by a factor of $1+G$. However, to simplify comparison of our model landscapes with existing data sets[18], we utilize the conventional $k_{sn} = A^{\frac{m}{n}}S$. Extended Data Fig. 9h shows the steepness index of the whole model domain as swath profile, with the median of values as bold line. Swath boundaries represent whisker-caps of a standard box-and-whisker plot of along-strike model data.

Code Availability

Numerical models are computed with published methods and codes, described in the Methods section and supplementary file. The code for longitudinality index calculations is available from the corresponding author on request.

Data Availability

All data supporting the findings of this study are contained within the article and supplementary files.

52. Harel, M.-A., Mudd, S. & Attal, M. Global analysis of the stream power law parameters based on worldwide 10Be denudation rates. *Geomorphology* **268,** 184–196 (2016).

53. Stock, J. D. & Montgomery, D. R. Geologic constraints on bedrock river incision using the stream power law. *Journal of Geophysical Research: Solid Earth* **104,** 4983–4993 (1999).

54. Guerit, L. *et al.* Fluvial landscape evolution controlled by the sediment deposition coefficient: Estimation from experimental and natural landscapes. *Geology* **47,** 853–856 (2019).

55. Densmore, A. L., Allen, P. A. & Simpson, G. Development and response of a coupled catchment fan system under changing tectonic and climatic forcing. *Journal of Geophysical Research - Earth Sciences* **112** (2007).

56. Armitage, J. J., Jones, T. D., Duller, R. A., Whittaker, A. C. & Allen, P. A. Temporal buffering of climate-driven sediment flux cycles by transient catchment response. *Earth and Planetary Science Letters* **369,** 200–210 (2013).

57. England, P. & McKenzie, D. A Thin Viscous Sheet Model for Continental Deformation. *Geophysical Journal of the Royal Astronomical Society* **70,** 295–321 (1982).

58. England, P. & McKenzie, D. Correction to - a Thin Viscous Sheet Model for Continental Deformation. *Geophysical Journal of the Royal Astronomical Society* **73,** 523–532 (1983).

59. Wobus, C. *et al.* in *Tectonics, Climate, and Landscape Evolution* (Geological Society of America, 2006).

60. Gleason, G. C. & Tullis, J. A Flow Law for Dislocation Creep of Quartz Aggregates Determined with the Molten-Salt Cell. *Tectonophysics* **247,** 1–23 (1995).

61. Mackwell, S. J., Zimmerman, M. E. & Kohlstedt, D. L. High-temperature deformation of dry diabase with application to tectonics on Venus. *Journal of Geophysical Research-Solid Earth* **103,** 975–984 (1998).

62. Karato, S. & Wu, P. Rheology of the Upper Mantle - a Synthesis. *Science* **260,** 771–778 (1993).

63. Owens, T. J. & Zandt, G. Implications of crustal property variations for models of Tibetan plateau evolution. *Nature* **387,** 37–43 (1997).

Acknowledgements

S.G.W. and X.Y. acknowledge support from TOTAL through the COLORS project. Chris Beaumont is thoroughly thanked for constructive comments on an earlier version of the scaling analysis developed here and for proposing to introduce the Surface Processes Damköhler numbers.

Author Contributions

S.G.W., R.S.H., J.B., and X.Y. designed the experiments, discussed the results and implications, and wrote the article. With help from R.S.H., J.B. and X.Y., S.G.W. developed the coupling between the tectonic model and the surface process model. S.G.W. conducted the comparison to Nature, and run and visualized the models.

Additional information

Supplementary Information is available for this paper. Correspondence and requests for materials should be addressed to S.G.W. at sebastian.wolf@uib.no. Reprints and permissions information is available at www.nature.com/reprints.

Competing interests

The authors declare no competing interests.

Extended Data Figures

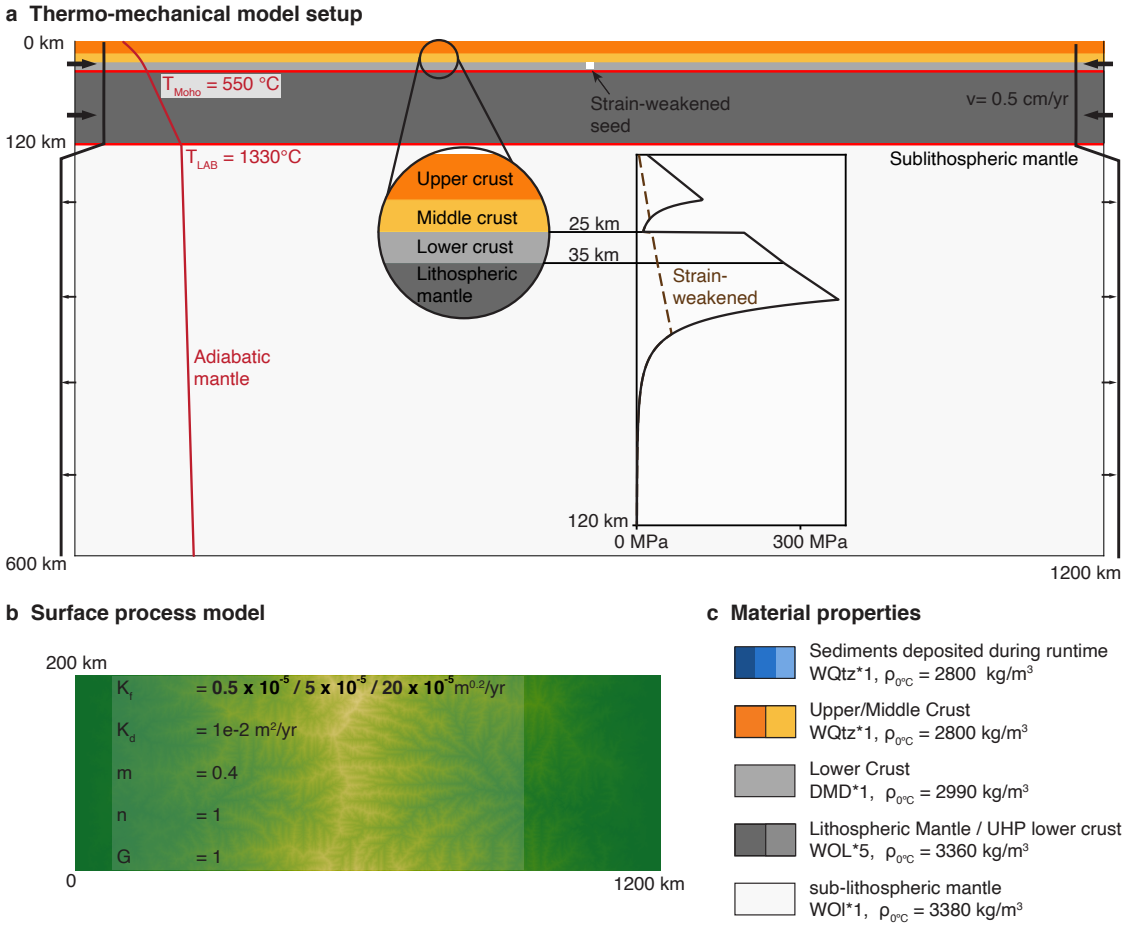

Extended Data Figure 1 | Model setup with boundary conditions (a), initial landscape with surface process parameters (b), and material legend with properties (c). a, The model is 1200 km wide, 600 km deep and has a uniform layered material distribution. A zoom into the continental lithosphere with corresponding yield-strength-envelope is shown as insert. Mountain building is modelled by applying a velocity boundary condition on both model sides in the lithosphere. Inflow is balanced by small distributed outflow of material in the sub-lithospheric mantle. The side and lower model boundaries have free slip conditions and the upper surface is free. The thermo-mechanical model is coupled to the surface process model FastScape, which starts out with a fluvial network with maximum 250 m elevation (**b**). The free surface corresponds to the average FastScape elevation. The initial temperature distribution in the continent corresponds to 1D-thermal steady state and the temperature in the sub-lithospheric mantle follows an adiabatic gradient of 0.4 °C. The side boundaries are insulated and the top and bottom of the model domain have fixed temperatures with respectively 0 °C and 1522 °C. **c**, Material legend shows colour, scaled flow law, and density of model materials. Blues for syn-contractional sediments alternate every 5 Myr. WQtz is the wet quartz flow law from Gleason & Tullis [60], DMD is dry Maryland flow law from Mackwell *et al.* [61], WOl is the wet olivine flow law from Karato & Wu [62].

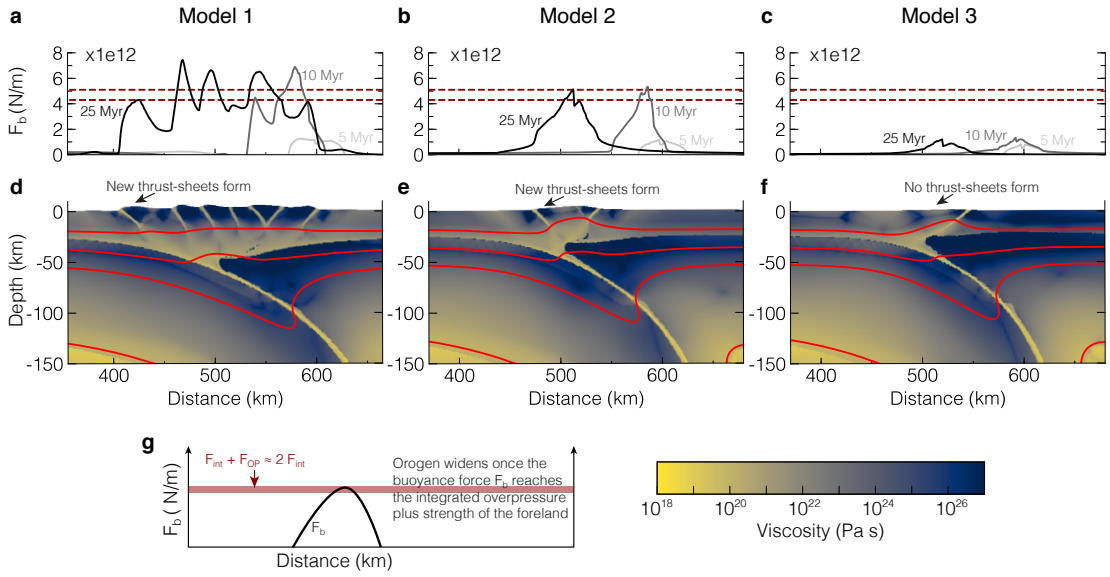

Extended Data Figure 2 | Evolution of Bouyancy Forces. a-c, Buoyancy force plots for three different timesteps with explanation in (**g**). The plots shows the computed buoyancy force as black/grey lines and the sum of integrated overpressure $\bar{P}_O$ plus F_{int} as red stippled lines. The stippled lines frame a typical range of values computed in the foreland crustal column in models 1 and 2, at several timesteps. On average, $\bar{P}_O \approx F_{int}$. **d-f**, Viscosity field and temperature contours (red) at the end of the shortening phase (25 Myr).

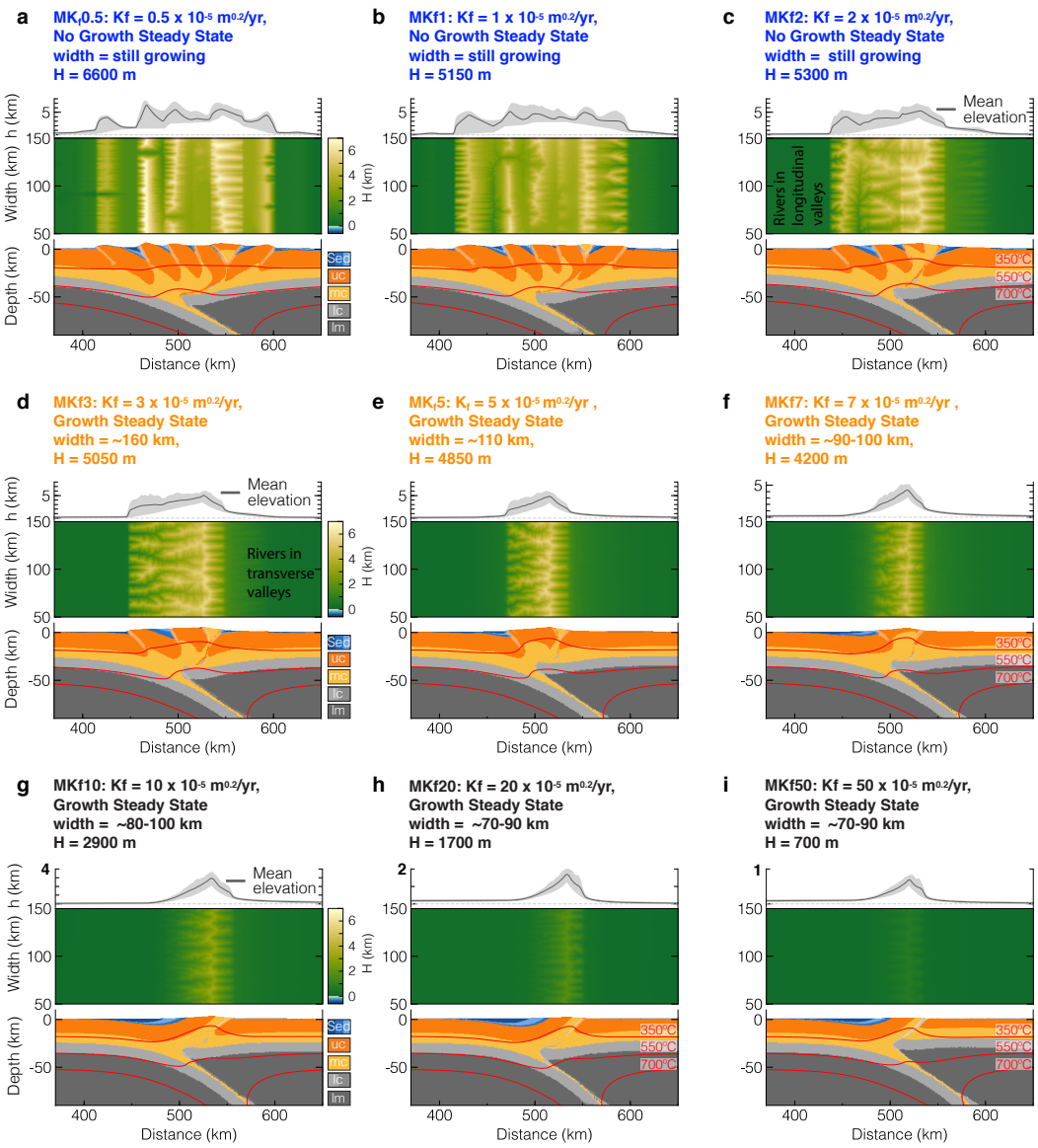

Extended Data Figure 3 | Supplementary growth-only models with variable fluvial erodibility. a-i, Snapshots of supplementary models 1-9 after 25 Myr of model evolution. Each panel consists of: Zoom into the model domain showing material distribution and temperature contours of thermo-mechanical tectonic model, map-view landscape from landscape evolution model FastScape, and swath elevation profile of the landscape. Swath profiles have the same scale in a-f, but a different scale in g-i. Top-row models do not reach flux steady state (Type 1); middle-row models reach steady state and are to first order strength-limited (Type 2); bottom-row models reach flux steady state and are erosion-limited (Type 3). Note: Non steady state models exhibit rivers flowing in longitudinal valleys in orogen core, and erosion-limited orogens do not form thrust sheets on the left side. H is the maximum mean elevation plotted as function of time in Extended Data Fig. 4b. Colours of model titles a-i correspond to colours in Extended Data Fig. 4.

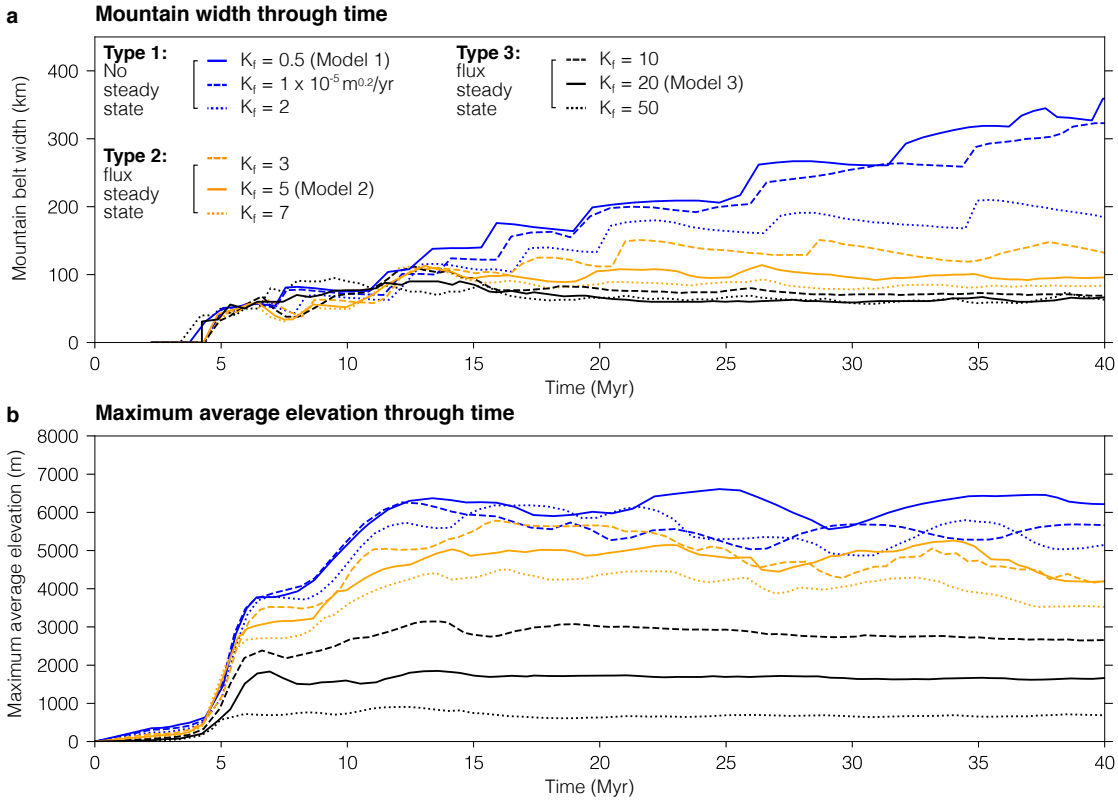

Extended Data Figure 4 | Time-dependent evolution of mountain width and height. a,b, Evolution of mountain width and maximum mean elevation through time for the 9 growth-only models with different fluvial erodibility shown in Extended Data Fig. 3. The mountain width is calculated every 0.5 Myrs between the two outermost points above 600 m, or above 15 % of maximum mean height (black Type 3 models). Steps in width correspond to new outward-propagating thrusts.

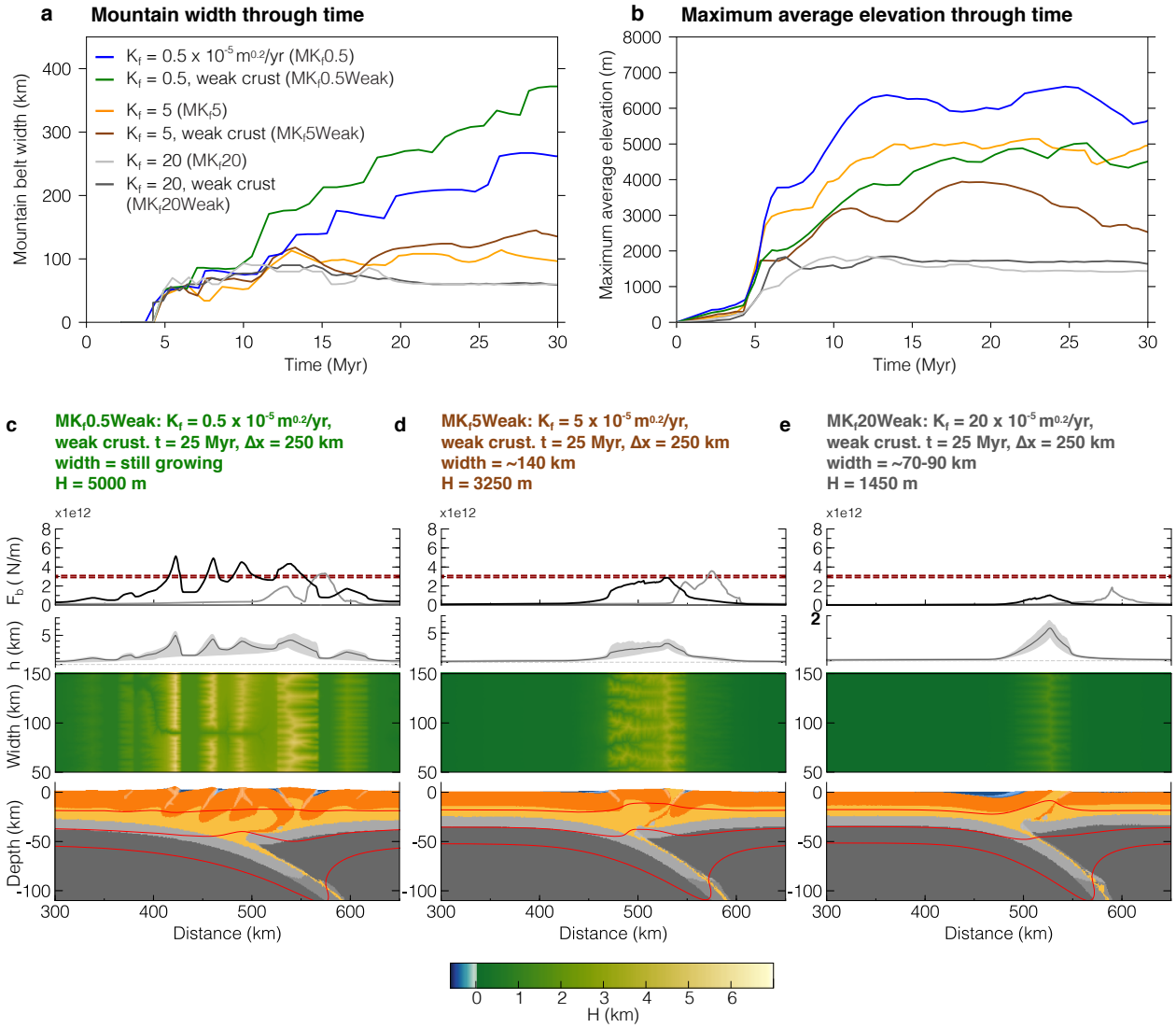

Extended Data Figure 5 | The influence of crustal rheology. **a,b**, Evolution of mountain width and maximum mean elevation through time for three models with different fluvial erodibility and low crustal strength. Colours are the same in both plots. Mountain width is calculated every 0.5 Myrs between the two outermost points which are above 600 m, or above 15 % of maximum mean height (in MK_f20 and $MK_f20Weak$). Steps in width correspond to new outward-propagating thrusts. **c-e**, Snapshots of models $MK_f0.5Weak$, MK_f5Weak, and $MK_f20Weak$ after 25 Myr of model evolution. Each panel consists of: Zoom into the model domain showing material distribution and temperature contours of thermo-mechanical tectonic model (see Extended Data Figure 1 for material colours), map-view landscape from landscape evolution model FastScape, swath elevation profile of the landscape, and buoyancy force plot. The buoyancy force plot shows one earlier timestep (10 Myr) as a grey line and the sum of integrated overpressure $\bar{P}_O$ plus F_{int} as red stippled lines. The stippled lines frame a typical range of measured values. On average $\bar{P}_O \approx F_{int}$; $\bar{P}_O$ and F_{int} are computed in the foreland crustal column in models $MK_f0.5Weak$ and MK_f5Weak, at several timesteps.

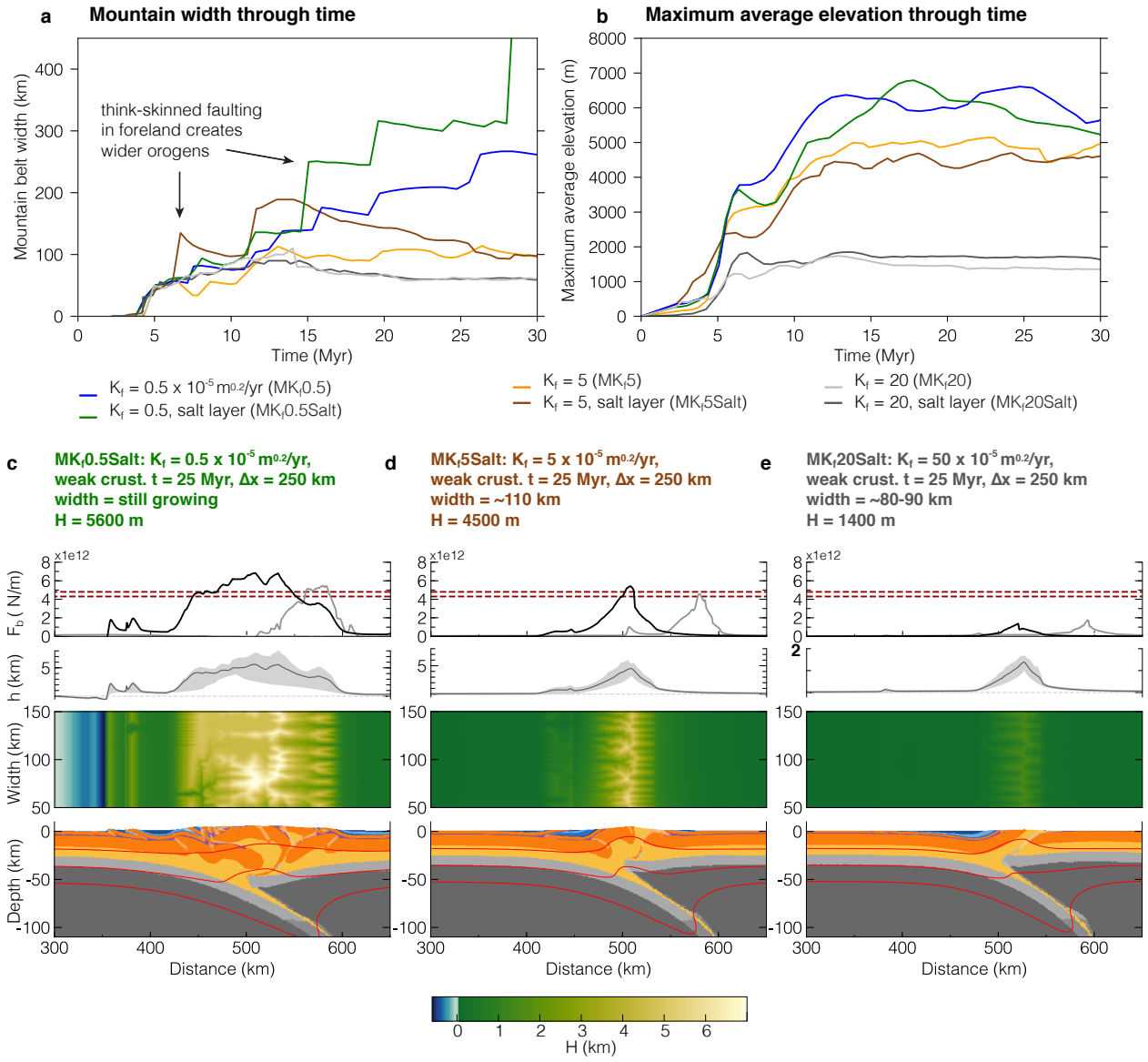

Extended Data Figure 6 | Influence of variable structural style (decoupled thick- and thin-skinned tectonics). a,b, Evolution of mountain width and maximum mean elevation through time for three models with different fluvial erodibility and with shallow crustal decoupling horizon ("salt" layer). Colours are the same in both plots. The mountain width is calculated every 0.5 Myrs between the two outermost points above 600 m, or above 15 % of maximum mean height (in MK_f20 and $MK_f20Salt$). Steps in width correspond to new outward-propagating thrusts. **c-e**, Snapshots of models $MK_f0.5Salt$, MK_f5Salt, and $MK_f20Salt$ after 25 Myr of model evolution. Each panel consists of: Zoom into the model domain showing material distribution and temperature contours of thermo-mechanical tectonic model (see Extended Data Figure 1 for material colours, purple is the weak layer), map-view landscape from landscape evolution model FastScape, swath elevation profile of the landscape, and buoyancy force plot. The buoyancy force plot shows one earlier timestep (10 Myr) as a grey line and the sum of integrated overpressure $\bar{P}_O$ plus F_{int} as red stippled lines. The stippled lines frame a typical range of measured values. On average, $\bar{P}_O \approx F_{int}$; $\bar{P}_O$ and F_{int} are computed in the foreland crustal column in models $MK_f0.5Salt$ and MK_f5Salt, at several timesteps.

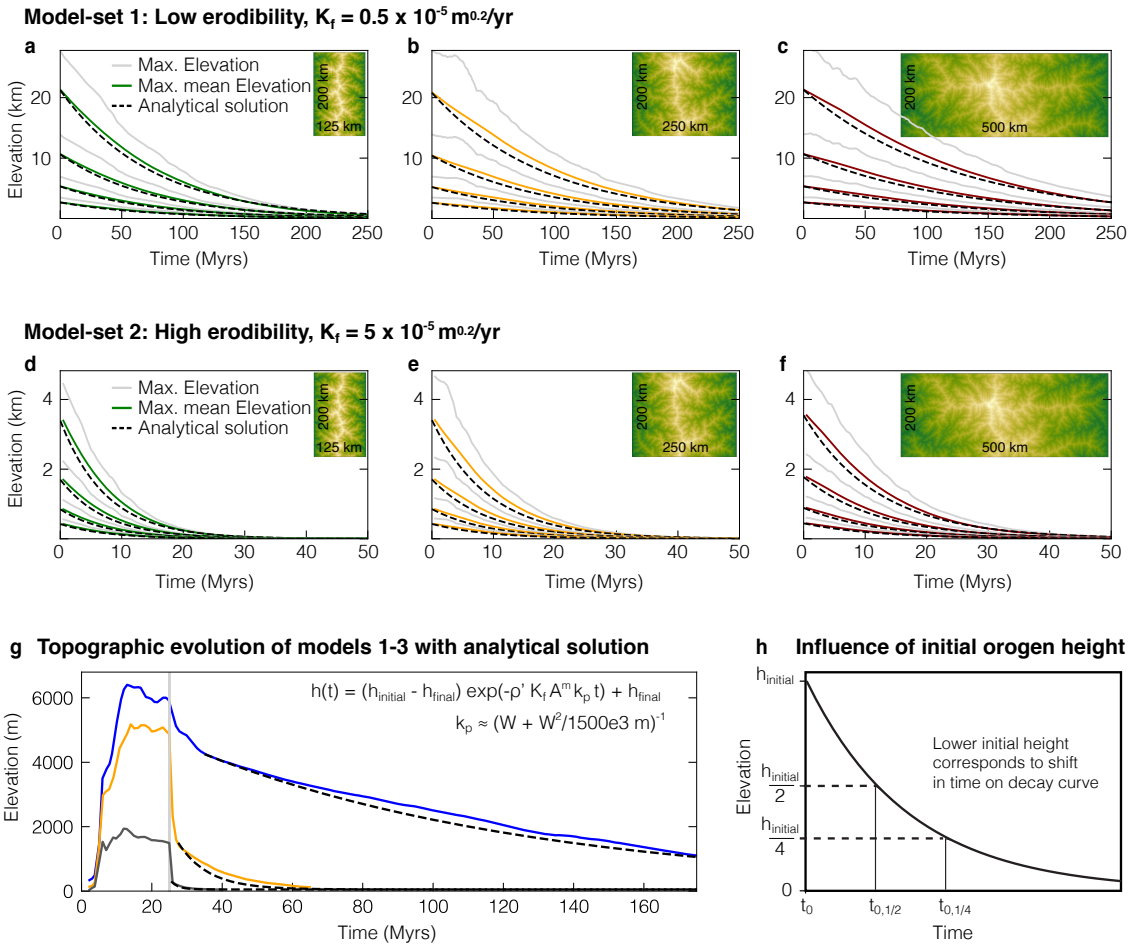

Extended Data Figure 7 | Analytical scaling relationship for decay phase II - effectively local isostatic rebound. a-f, Elevation-time plots of FastScape-only models with low and high erodibility, variable orogen width and variable initial orogen height. Each sub-figure shows the evolution of topography and corresponding analytical solution of four models starting with the same width but with different initial heights. Uplift in these models is local-isostatic ($U = (1 - \rho') \times \dot{e}$), erosion follows the (extended) stream-power law with the same parameters as used in the coupled models. **g**, Shows evolution of maximum mean topography of the three models presented in the main text (Figure 1) with corresponding analytical solutions. The analytical solution is derived in the supplemental material. We see that a wider orogen and lower erodibility lead to slower decay; a lower initial starting height corresponds to a shift in time on the decay curve. The latter is displayed in (**h**). All models show good fit between analytical solution and evolution of topography.

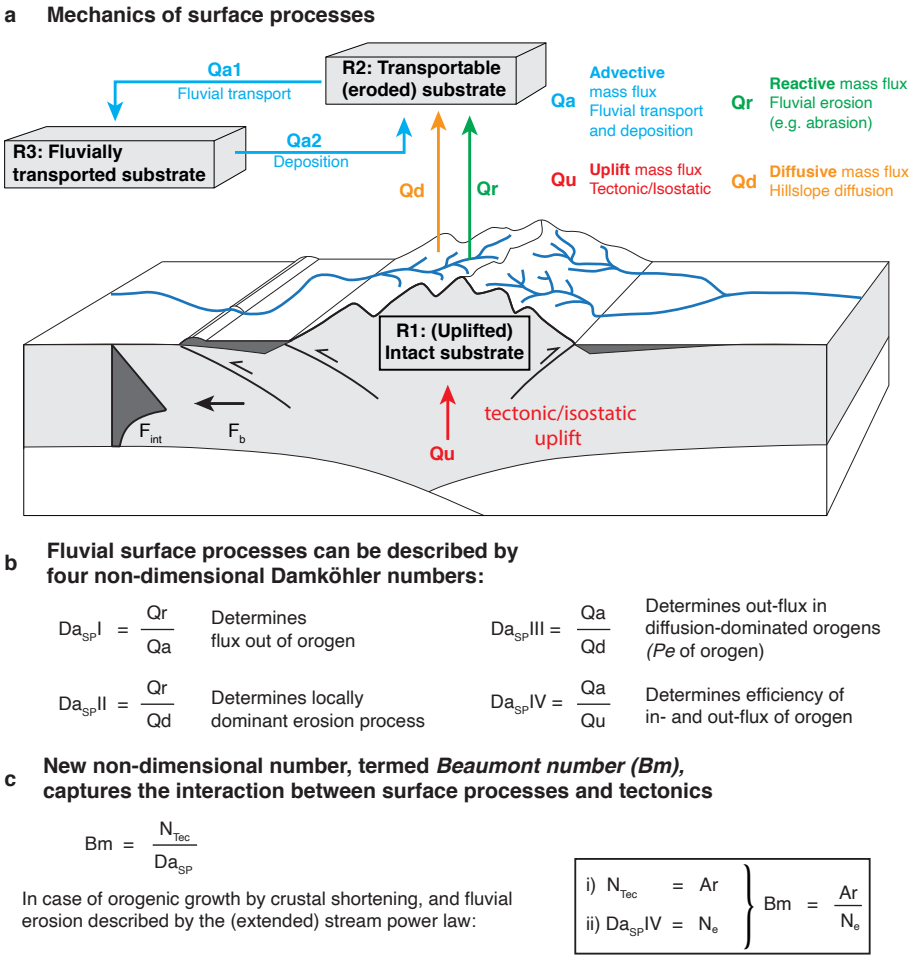

Extended Data Figure 8 | Non-dimensional Surface Processes Damköhler numbers and Beaumont number. a, Theoretical box model that describes the mechanics of surface processes with fluxes between different hypothetical reservoirs. **b**, Definition of the four Surface Processes Damköhler numbers (Da_{SP}) determining the mechanics and efficiency of surface processes. **c**, Definition of a new non-dimensional number, termed Beaumont-number (Bm) that determines the interaction between surface processes and tectonics. N_{Tec} is the non-dimensional number determining topographic growth, here the crustal Argand number Ar in case of collisional orogens, N_e is the uplift-erosion number.

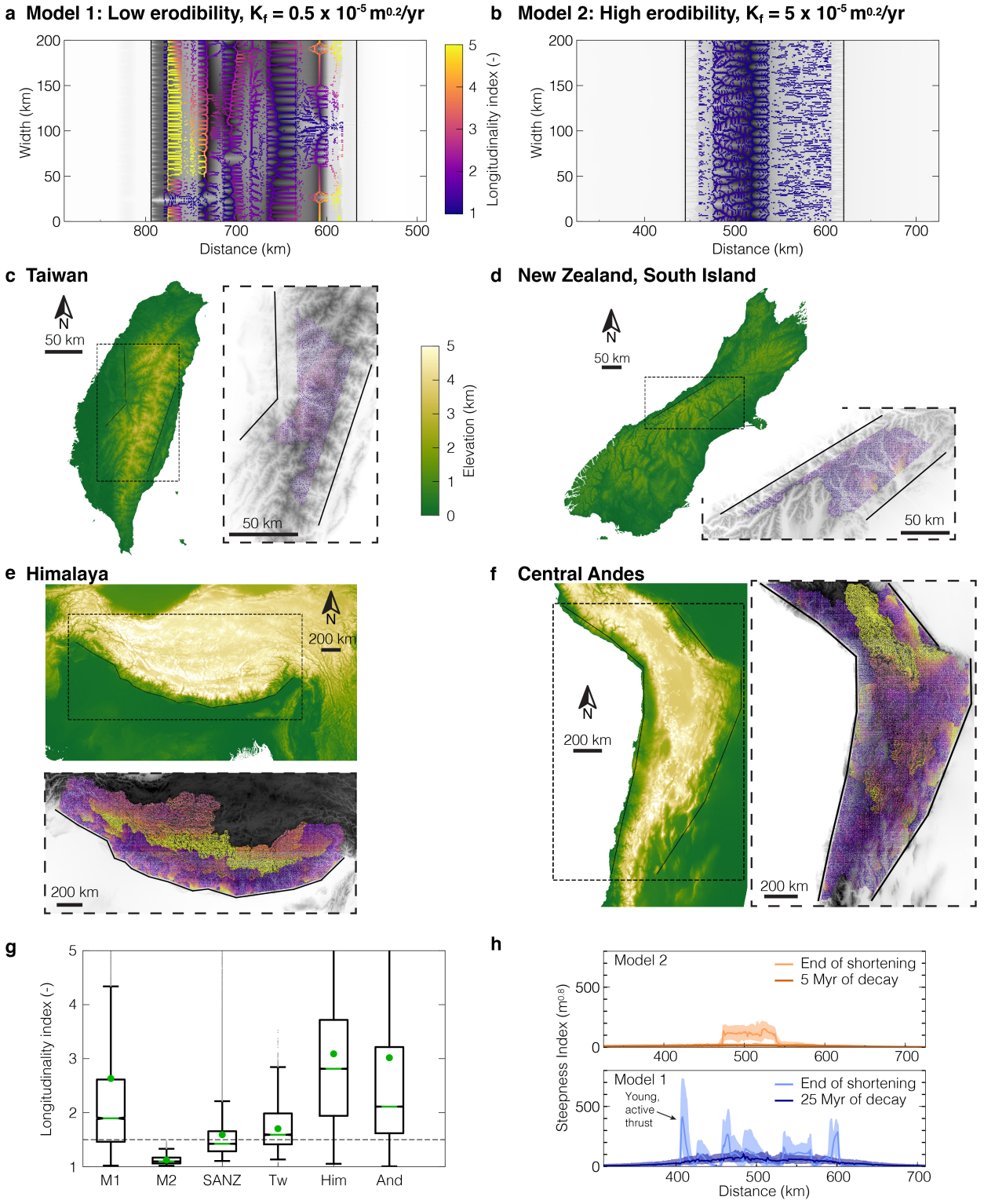

Extended Data Figure 9 | Longitudinality index in modelled orogens (a,b) and natural examples (d-f), steepness index of modelled orogens (h). **a,b**, 2D longitudinality index (LI) plots of Models 1 and 2 showing the FastScape elevation as grey-shade in the background, the LI of each source point ($A = 1 \times 10^5\,\mathrm{m}^2$) of a river as colour coding, and the corresponding rivers as light-grey and transparent overlay. The black lines are the orogen boundaries corresponding to 300 m average elevation. **c-f**, DEM and (LI) plots for Taiwan (Tw), the Southern Alps of New Zealand (SANZ), Himalaya-Tibet (Him), and the Central Andes (And). The DEMs show elevation as colour coding, the manually picked orogen boundaries as black lines, and a stippled box outlining the LI plots. The LI plots show elevation as grey-shade in the background, each LI of a source point ($A = 1 \times 10^5\,\mathrm{m}^2$) of a river as colour coding. **g**, Box-and-whisker plots show the full LI

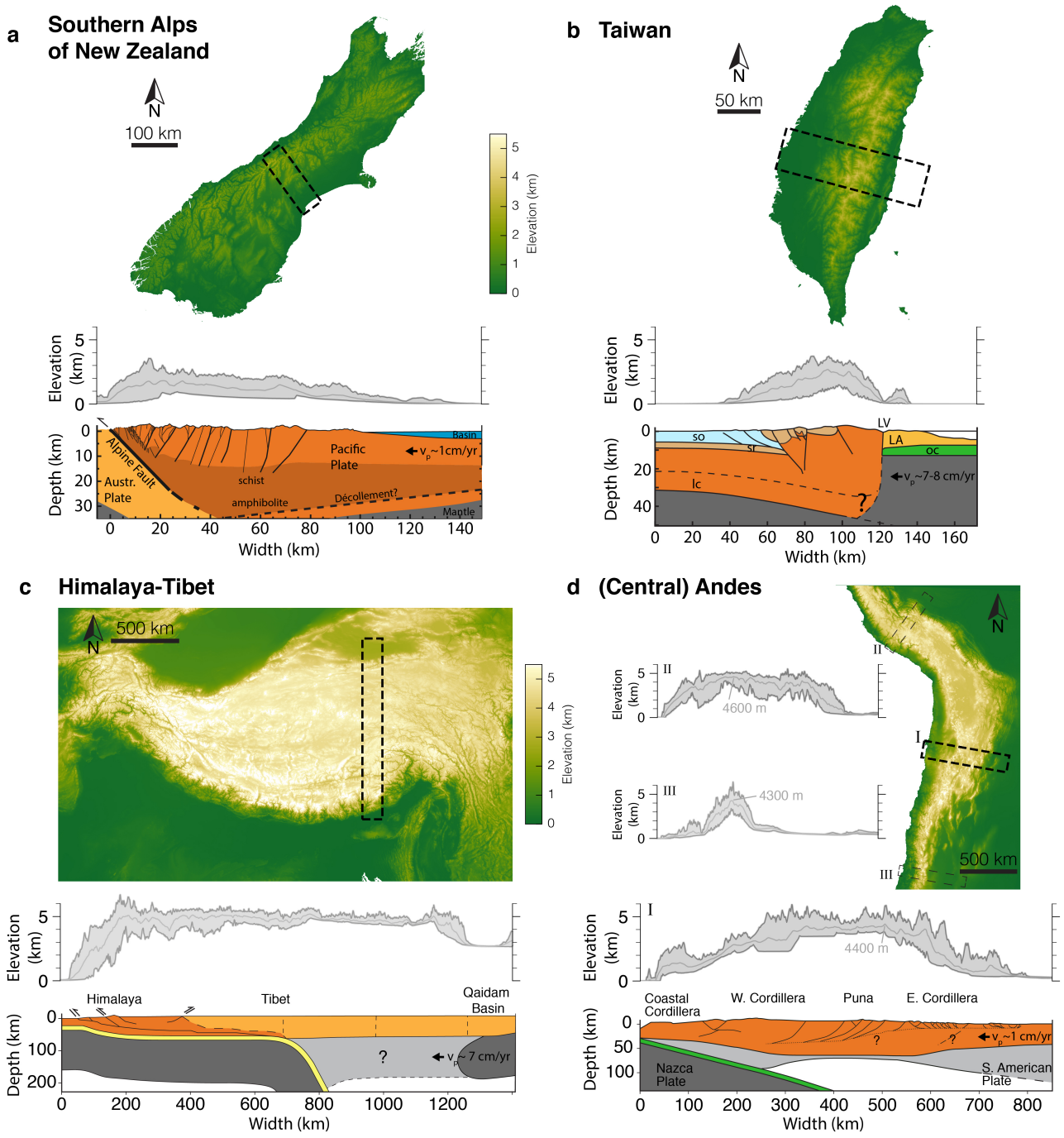

Extended Data Figure 10 | Digital elevation models, swath profiles, and geological cross sections of the Southern Alps of New Zealand, Taiwan, Himalaya-Tibet and Central Andes. Swath profiles are created in the vicinity of the cross sections, oranges are crust, greys are lithospheric mantle, and v_c is the convergence velocity related to crustal thickening. **a**, Cross section modified from Little [34] and Herman *et al.* [36]. **b**, Cross section modified from Brown *et al.* [38] and Van Avendonk *et al.* [41]. *lc* is lower crust, *oc* is oceanic crust, *so* are syn-orogenic sediments, *sr* are pre-orogenic syn-rift sediments, LA is the Luzon Arc, LV is the longitudinal valley, orange color is crustal rocks. **c**, Cross section modified from Owens & Zandt [63]. Yellow color is lower crust, orange is crust from the pro-plate, light-orange is Tibetan retro-plate crust. The light-grey lithospheric mantle is possibly removed. **d**, Cross section modified from DeCelles *et al.* [42]. The additional swath profiles II and III show that the actively shortening Central Andes reach similar heights independent of orogen width.

Supplementary Information for: Topography of mountain belts controlled by rheology and surface processes

Sebastian G. Wolf[1], Ritske S. Huismans[1], Jean Braun[2,3], Xiaoping Yuan[4,2]

[1]*University of Bergen, Department of Earth Science, Bergen, Norway*
[2]*Helmholtz Centre Potsdam, German Research Centre for Geosciences, Potsdam, Germany*
[3]*Institute of Geosciences, University of Potsdam, Potsdam, Germany*
[4]*Hubei Key Laboratory of Critical Zone Evolution, School of Earth Sciences, China University of Geosciences, Wuhan, China*

Content

This supplementary file contains:

- An explanation of the supplementary model animations.
- An extended Methods sections explaining the modelling basics and setup choices of the thermo-mechanical-landscape-evolution model.
- A detailed description of the supplementary models.
- The derivation of the scaling relationship between surface processes and tectonics during orogenic growth.
- A comprehensive comparison between model inferences and the natural examples discussed in the text.
- The derivation of the scaling relationship between surface processes and tectonics during orogenic decay.

1 Model Animations

The data repository contains 21 animations of the main end-member models M1-M3 and the supplementary models. M1-M3 are displayed in 3D-view with the thermo-mechanical model in the bottom, and the landscape evolution model on top. M1-M3 and all supplementary models are furthermore presented in animations consisting of four subplots showing from

top to bottom: Uplift and average erosion rate, Average elevation with swath profile, 2D FastScape surface, and the FANTOM material colors (see legend in Extended Data Fig. 1) with temperature contours (100 °C, 350 °C, 550 °C, 700 °C). Naming of supplementary animations follows the same convention as used in the article.

2 Supplementary Methods

2.1 Thermo-mechanical model

2.1.1 Basic principles

We use the extended 2-dimensional Arbitrary Langrangian-Eulerian (ALE), finite element tectonic model FANTOM[1,2], coupled to the landscape evolution model FastScape[3,4], to investigate the topographic evolution of mountain belts during growth and decay. The thermo-mechanical model FANTOM solves momentum and mass conservation (eqs. S1, S2) of plane-strain incompressible creeping materials, and heat transfer (eq. S3) in the model domain:

$$\frac{\partial \sigma_{ij}}{\partial x_i} + \rho g = 0 \quad i,j = 1,2, \tag{S1}$$

$$\frac{\partial v_i}{\partial x_i} = 0 \quad i = 1,2, \tag{S2}$$

$$c_p \rho \left(\frac{\partial T}{\partial t} + v_i \frac{\partial T}{\partial x_i} \right) = k \frac{\partial}{\partial x_i} \frac{\partial T}{\partial x_i} + H + v_j \alpha \rho T g, \tag{S3}$$

where v_i are velocity components, x_i are spatial coordinates, σ_{ij} is the stress tensor, ρ is density, g is gravitational acceleration, c_p is specific heat, T is temperature, t is time, k is thermal conductivity, H is radioactive heat production per unit volume, and α is the volumetric thermal expansion coefficient. The term $v_j \alpha \rho T g$ in eq. S3 is the correction for adiabatic heating and cooling when material moves vertically. Density, ρ, is a function of temperature through $\rho(T) = \rho_0 (1 - \alpha (T - T_0))$, where α is the coefficient of thermal expansion.

Model materials deform either by viscous or frictional-plastic flow. Frictional-plasticity is modelled using a pressure-dependent Drucker-Prager yield criterion:

$$\sigma'_{plast} = P \cdot \sin(\phi_{eff}) + C \cdot \cos(\phi_{eff}), \tag{S4}$$

where σ'_{plast} is the square root of the second invariant of the deviatoric stress, P is the dynamic pressure, ϕ_{eff} is the effective angle of internal friction and C is cohesion. Gouge

formation, mineral reactions[5], and fluid pressure variations[6] typically weaken fault zones on Earth. In our modelling approach we approximate these processes by linearly reducing the effective angle of internal friction ϕ_{eff} from 15° to 2° and C from 20 MPa to 4 MPa within a pre-defined strain-interval $0.1 < \epsilon_{plastic} < 1.1$ [7]. Note that $\phi_{eff} = 15°$ corresponds approximately to hydrostatic pore-fluid-pressure conditions.

When the deviatoric stress is below σ'_{plast}, model materials deform by a non-linear, thermally-activated power law creep, which relates pressure, temperature and strain rate to the viscous flow stress, σ'_{visc}:

$$\sigma'_{visc} = f \cdot A^{-\frac{1}{n}} \cdot (\dot{\epsilon}_{eff})^{\frac{1}{n}} \cdot exp\left(\frac{Q + VP}{nRT}\right), \tag{S5}$$

where σ'_{visc} is the square root of the second invariant of the deviatoric stress, $\dot{\epsilon}_{eff}$ is the square root of the second invariant of the deviatoric strain rate, f is a scaling factor, A the pre-exponential factor converted to plane strain, n the power-law exponent, Q the activation energy, V the activation volume, P the dynamic pressure, and R the universal gas constant.

2.1.2 Model setup

Continent-continent collision is modelled in an idealised upper mantle-scale Cartesian cross-section with 600 km vertical and 1200 km horizontal extent (Extended Data Fig. 1). The model domain has a layered material distribution consisting of 25 km upper/middle crust, 10 km lower crust, 85 km of lithospheric mantle down to 120 km depth, underlain by sub-lithospheric mantle to the lower boundary. Sediments deposited during runtime have the same properties as upper/mid crust but are marked by three different blue colours changing every 5 Myr. All materials are described by the same frictional-plastic parameters, subject to strain-weakening as a function of plastic strain. Viscous flow of upper/middle crust is described by a 'wet' quartz flow law[8], and lower crust follows a 'dry' Maryland diabase flow law[9]. The lithospheric mantle is described by a 'wet' olivine flow law[10], scaled by a factor $f = 5$ to account for strong, melt-depleted conditions. Sub-lithospheric mantle follows the same flow law scaled by $f = 1$. We use the scaling factor f to base our model materials on a minimum number of well established flow laws, while also accounting for extrapolation uncertainties from laboratory to nature and different geological situations.

The initial temperature field in the model domain is at steady state and represents typical average values for Phanerozoic lithosphere[11], with a Moho temperature of 550 °C at 35 km depth and 1330 °C at the lithosphere-asthenosphere boundary at 120 km depth, leading to heat flow of 53 mW m^{-2} at the surface and 20.8 mW m^{-2} in the sub-lithospheric mantle. To maintain the heat flux at the base of the lithosphere, resembling mantle convection at high Nusselt number, k linearly increases from 2.25 W m^{-1} K^{-1} to 52.0 W m^{-1} K^{-1} between 1330 and 1340 °C in the sub-lithospheric mantle[12]. This setup is designed to keep an adiabatic

gradient of $0.4\,^{\circ}\mathrm{C\,km^{-1}}$ in the sub-lithospheric domain. The top and bottom model domain boundaries have a constant temperature boundary condition of 0 °C and 1522 °C respectively, and the side boundaries are insulated.

Mountain growth and decay is modelled by applying inflow velocity boundary conditions of 0.5 cm/yr in the lithosphere on both sides. Inflow is balanced by outflow in the sub-lithospheric mantle (Extended Data Fig. 1). The velocity boundary conditions are applied for 25 Myr, creating a mountain belt with 250 km of shortening. Subsequently, inflow/outflow boundary conditions are switched off during mountain belt decay. The side boundaries have vertical roller conditions, the top surface is a true free surface and the bottom boundary is characterized by free slip.

The thermal and rheological setup leads to viscous decoupling of the upper/mid crust on top of the lower crust in discrete thick-skinned fault blocks. This specific setup is motivated by the Pyrenees, Alps, Taiwan, the Southern Alps of New Zealand, and Himalaya-Tibet, here at least the Indian plate which all exhibit viscous decoupling on top of the subducting lower crust and lithospheric mantle[13–21]. The effect of additional thin-skinned deformation on the evolution of mountain belt topography is tested in a set of supplementary models with a weak and shallow décollement level (Extended Data Fig. 6). During initial shortening a conjugate set of shear zones forms where randomly one branch is a tiny bit weaker than the other. Strain-weakening of the weaker branch provides a positive feedback leading to preferential localisation on one shear zone and large scale asymmetry with one-sided subduction of lithospheric mantle and lower crust. To simplify model comparison, models are flipped left-right during post processing in case the right lithospheric mantle subducts.

Material densities have common values (see Extended Data Fig. 1, Supplementary Table 1). The lithospheric mantle is depleted by $20\,\mathrm{kg\,m^{-3}}$ with respect to the underlying sub-lithospheric mantle. The depletion is representative for Phanerozoic lithospheric mantle[22,23], and leads to a near neutral buoyancy contrast between the subducting lithospheric mantle and the sub-lithospheric mantle. The model includes an irreversible metamorphic phase change of the strong mafic lower crust at UHP-conditions, following the phase diagram of Hacker [24]. For simplicity, the UHP equivalent has the same properties as lithospheric mantle. The metamorphosed lower crust is also subject to viscous strain-weakening by reducing the scaling factor from $f = 5$ to $f = 0.1$ within the strain interval $0.1 < \epsilon_{viscous} < 1.1$. Viscous weakening is limited by the 1000 °C isotherm and ensures proper decoupling between subducting and overriding plate.

The Eulerian grid consists of 1200 cells in horizontal and 264 cells in vertical direction. The distribution of cells is vertically non-uniform leading to a resolution of 250 m in the upper 20 km, 1 km to a depth of 160 km and 10 km in the remaining sub-lithospheric mantle. The horizontal resolution is constant with 1 km per cell.

Supplementary Table 1 | Mechanical and thermal properties of model materials.

Parameters	Sediments, Upper & middle crust	Lower crust	Mantle lithosphere	Sub-lithospheric mantle
Plastic rheology				
C - C_{sw} (MPa)	20-4	20-4	20-4	20-4
ϕ - ϕ_{sw} (°)	15-2	15-2	15-2	15-2
Viscous rheology				
Flow law[a]	WQtz	DMD	WOl	WOl
f	1	1	5	1
A ($Pa\,s^{1/n}$)[b]	8.57×10^{-28}	5.78×10^{-27}	1.76×10^{-14}	1.76×10^{-14}
n	4.0	4.7	3.0	3.0
Q ($kJ\ mol^{-1}$)	223	485	430	430
V ($cm^3\,mol^{-1}$)	0	0	10×10^{-6}	10×10^{-6}
Density				
ρ_0 ($kg\,m^{-3}$)	2800	2990 (3360)[c]	3360	3380
α (K^{-1})	3×10^{-5}	3×10^{-5}	3×10^{-5}	3×10^{-5}
Thermal				
k ($W\,m^{-1}\,K^{-1}$)[d]	2.25	2.25	2.25	2.25
H ($\mu W\ m^{-3}$)	1.15	0.5	0	0
c_p ($J\,kg^{-1}\ K$)[e]	804	762	682	1250

[a] WQtz is the wet quartz flow law as described in Gleason & Tullis [8]; DMD is the dry Maryland flow law from Mackwell *et al.* [9]; WOl is the wet olivine flow law from Karato & Wu [10].

[b] The laboratory derived pre-exponential flow law constant has been converted to conform with the second invariants of the stress and strain rates used in the model approach.

[c] Metamorphic UHP equivalent. The P-T-field for the metamorphic reaction coincides with the UHP-eclogite stability field from Hacker [24].

[d] Thermal conductivity for low temperatures. Between 1335 °C and 1345 °C the conductivity linearly increases from 2.25 to 52.0 $W\,m^{-1}\,K^{-1}$, to mimic active mantle convection at high Nusselt number, keep the adiabatic gradient and prevent the system from cooling.

[e] c_p is scaled to give uniform diffusivity of $1 \times 10^{-6}\,m^2/s$.

2.2 Landscape evolution model

To model surface processes we use the 2-dimensional, $O(N)$ and implicit, landscape evolution model FastScape[3], which is extended by taking into account sediment deposition[4]:

$$\frac{\partial h}{\partial t} = U - K_f A^m S^n + K_d \nabla^2 h + \frac{G}{A} \int_A \left(U - \frac{\partial h}{\partial t}\right) dA, \tag{S6}$$

where h is topographic elevation, t is time, U is uplift rate, K_f is the fluvial erodibility, A is the catchment area, S is the local slope, K_d is the hillslope diffusion coefficient, G is the dimensionless deposition coefficient, and m and n are the stream power exponents. The landscape evolution model computes changes in topography as a function of uplift, stream-power erosion (K_f-term), hillslope creep (K_d-term), and continental deposition as a function of the net erosion upstream (G-term). The model predicts the smooth transition between detachment-limited and transport-limited behaviors. Local minima, i.e. lakes and also the orogenic foreland basins, are filled up from the deepest point with the locally available sediments. Every river is connected to either the left or right side boundary by bridging local minima to their lowest neighbour catchment.

2.3 Coupling between thermo-mechanical and landscape evolution model

The thermo-mechanical model FANTOM and the surface process model FastScape are coupled in a T-coupling manner[25]. After every thermo-mechanical timestep, the surface velocity is given to FastScape as a cylindrical signal. First, the landscape is advected horizontally according to the given velocity field. The vertical velocity field is subsequently used as input to solve the extended stream-power model (eq. S6). Next, the average surface elevation is given back as the new free surface of the thermo-mechanical model. Finally, any erosion or deposition is accounted for by removal or addition of marker particles in FANTOM. The FastScape surface sits truly on top of the thermo-mechanical model without any interpolation steps. Accordingly, the model domain is 1200 km wide and we chose a depth of 200 km. See below for more discussion of the FastScape model depth. The landscape evolution model has the same spatial resolution as the tectonic model (1 km) in both dimensions. The left and right side boundaries of the landscape are open so that water flows out, and the top and bottom boundaries are periodic. All models start with the same steady-state landscape which has a maximum height of 250 m (Extended Data Fig. 1b), resembling a pre-existing river system.

2.4 The influence and meaning of the FastScape model depth (y-dimension)

Tests with different depths of the FastScape model domain have shown that model evolution is not dependent on the depth of the surface processes model. The local minima bridging algorithm in FastScape ensures continuous water flow to the left and right side boundaries of the model domain. This leads automatically to cutting of newly forming thrusts, which explains why all thrusts in Model 1 are cut at least once by rivers. In Nature, thrusts are expected to have a finite along-strike extent and are not continuous features. Furthermore, rivers would either cut a newly forming thrust or flow around it if possible. Since all thrusts in FastScape are at least cut once due to local minima bridging, the FastScape model depth can be interpreted as representing a typical thrust length in Nature. We chose a FastScape model depth of 200 km because it represents a typical maximal thrust wavelength observed in different active mountain belts on Earth (see Extended Data Fig. 9, 10). A model width of 200 km also generates LI values comparable to natural mountain belts, which corroborates our value choice.

3 Description of supplementary models

3.1 The influence of fluvial erodibility

Nine supplementary models with variable K_f, longer growth phase (40 Myr, 400 km convergence), and without the decay phase highlight the influence of fluvial erodibility during growth (see Extended Data Figs. 3 and 4). Increasing K_f from $0.5 \times 10^{-5}\,\mathrm{m}^{0.2}/\mathrm{yr}$ to $2 \times 10^{-5}\,\mathrm{m}^{0.2}/\mathrm{yr}$, we see: a) the orogen widening rate is lower with higher K_f as growth is more efficiently counteracted by erosion, b) model orogens are still widening and thus not in flux steady state, c) rivers flow partly in longitudinal valleys, and d) maximum mean orogen height is lower in MK_f1 and MK_f2 than in $MK_f0.5$, but MK_f1 and MK_f2 have similar elevation. The increase from $K_f = 2 \times 10^{-5}\,\mathrm{m}^{0.2}/\mathrm{yr}$ to $K_f = 3 \times 10^{-5}\,\mathrm{m}^{0.2}/\mathrm{yr}$ marks the transition to flux steady state, because MK_f3 is on average not widening any more. The transition is also shown by the characteristic absence of thrust-related longitudinal valleys in MK_f3. Importantly, MK_f2 and MK_f3 have very similar maximum mean elevation through time, though MK_f3 is slightly lower (Extended Data Fig. 4). Increasing K_f from $3 \times 10^{-5}\,\mathrm{m}^{0.2}/\mathrm{yr}$ to $5 \times 10^{-5}\,\mathrm{m}^{0.2}/\mathrm{yr}$ notably changes orogen width from around 150 to 110 km. In terms of orogenic structures, MK_f3 is composed of 2-3 thrust sheets, while model MK_f5 is only composed of one to maximum two thrust sheets (Extended Data Figs. 3d,e). However, both models have a very similar maximum mean elevation through time (Extended Data Fig. 4). Increasing K_f even further to $7 \times 10^{-5}\,\mathrm{m}^{0.2}/\mathrm{yr}$, only marginally decreases orogen width, but significantly lowers the maximum mean elevation through time.

The mountain belt is furthermore only composed of one thick-skinned thrust sheet. Further increasing K_f up to $50 \times 10^{-5}\,\mathrm{m}^{0.2}/\mathrm{yr}$ significantly decreases orogen height, but the width stays roughly the same at around 80 to 90 km. Hence, increasing K_f in the models reaching flux steady state reduces orogen width while keeping a similar orogen height, until a certain width-limit (W_{min}) is reached. After the width-limit is reached, orogen height is reduced with increasing K_f, while the width roughly stays the same. The width-limit corresponds to one crustal thrust sheet. Additionally, once the width-limit is reached, no thrusts form any more on the pro-side of the orogen. Rather, the pro-side crust forms a monocline as described in model 3. We note that in the limit of extremely high K_f, minimum orogen width likely becomes sensitive to K_f. However, this situation would only result in orogens with few tens to hundred meters of average topography (compare to model with $K_f = 50 \times 10^{-5}\,\mathrm{m}^{0.2}/\mathrm{yr}$ that is 700 m high, Extended Data Fig. 3i), which is not common in Nature.

3.2 The influence of crustal strength

Three supplementary "growth-only" models (40 Myr run time, 400 km convergence) with lower crustal strength, but the same fluvial erodibilities as models 1 to 3, show the effect of crustal rheology on mountain height, width and structure (Extended Data Fig. 5). Lower crustal strength in model $MK_f0.5Weak$ than in $MK_f0.5$ results in efficient decoupling between middle crust and lower crust, creating slightly wider thrust sheets, variable thrust dips, and topography dominated by thrust-related blocks. The model orogen is also wider and lower in elevation than $MK_f0.5$ (Extended Data Fig. 5). The weak model with high fluvial erodibility (MK_f5Weak) has a similar crustal structure as its strong counterpart (MK_f5), and also reaches flux steady state, characterised by pre-dominantly transverse valleys. Also here, the orogen is wider and lower in elevation than MK_f5 (Extended Data Fig. 5). Lower crustal strength in model $MK_f20Weak$ has only a marginal effect on model development compared to model 3 (MK_f20). Both orogens reach similar width, height, and structure through time (Extended Data Fig. 5e). The buoyancy forces F_b and sum of $\bar{P}_O$ plus F_{int} also follow the same pattern as in models 1 to 3: $F_b \approx \bar{P}_O + F_{int}$ in models $MK_f0.5Weak$ and MK_f5Weak, and F_b does not reach the same values in $MK_f20Weak$. Note that $MK_f20Weak$ does not form thrusts on the pro-side.

3.3 The influence of variable structural style (decoupled thick- and thin-skinned tectonics)

Three supplementary "growth-only" models (40 Myr run time, 400 km convergence) with an additional, weak decoupling horizon initially at $3-4$ km depth (purple color), but the same fluvial erodibilities as in models 1 to 3, show the effect of decoupling between thick-and thin-skinned tectonics on mountain height, width and structure (Extended Data Fig. 6).

We observe that mountain height is not significantly changed by adding a weak decoupling horizon, although possibly a bit lower in MK_f5Salt than in MK_f5 (Extended Data Fig. 6b). Orogen width is larger and more variable in $MK_f0.5Salt$ and MK_f5Salt when including a weak salt decoupling level, because modelled orogens include a thin-skinned foreland fold-thrust belt. Furthermore, orogenic structure is notably influenced by decoupling between thin- and thick-skinned tectonics. Decoupling between thin- and thick-skinned deformation can also be observed in the surface expression of $MK_f0.5Salt$ and MK_f5Salt. Thin-skinned faults create several longitudinal valleys in the foreland-belts, and antiformal duplexing in the orogen core creates seemingly fewer longitudinal valleys than in the models without salt. Still, the absence of longitudinal valleys in the orogen core is to first order indicative for flux steady state in MK_f5Salt, certainly in $MK_f20Salt$ (Extended Data Figs. 6d,e).

4 Scaling orogenic growth

In this section, we derive generalizing scaling laws relating tectonics and surface processes during orogenic growth. First, we relate buoyancy forces to plate strength. The relationship explains the maximum average elevation of modelled orogens, and allows subdividing orogens into three different types. Second, we define a framework of non-dimensional numbers that describes the dynamics of (fluvial) surface processes. Third, we define a new non-dimensional number, termed Beaumont-number (Bm) that relates key non-dimensional numbers of tectonic deformation and surface processes to create a generally applicable scaling relationship between surface processes and tectonics. Finally, we derive the Beaumont-number of modelled orogens.

4.1 The physics of orogen widening

4.1.1 Steady or non-steady state: The strength limit

Rheological control on maximum mean topography is readily understood to first order by considering a simple force balance, which is explained here and derived below. Shortening creates surface uplift, which raises the gravitational potential energy of the mountain belt, resulting in a force per metre orogen that the mountain belt exerts onto its foreland. Once this force exceeds the strength and overpressure of the crust, a new, outward-propagating thrust sheet forms (see Extended Data Fig. 2). Hence, once surface uplift reaches a rheologically controlled limit (h_R), a new thrust sheet forms. This implies that any outward growth happens at the rheologically controlled limit. In model 1 ($MK_f0.5$) we observe that any erosion in the orogen core is balanced by surface uplift. Hence, the orogen not only grows towards h_R with newly forming thrusts, but also reactivates old, internal thrusts as response

Supplementary Table 2 | Symbols in alphabetical order used in the derivation of the scaling relationship between tectonics and surface processes; related equations and common values are shown if applicable.

Symbol	Explanation	Related equations and common values used in computations
Related to tectonics		
Ar	Argand number (crustal)	$Ar = \frac{\rho_c \rho' g h_{dec}^2}{F_{int}}$
β	Crustal thickening factor	
β_0	Maximum crustal thickening factor before orogen widening	$\beta_0 = \sqrt{\frac{4}{Ar} + 1}$
F_b	Buoyancy force (gravitational potential energy variation)	$F_b = \rho_c g H \left(h_{dec} + \frac{\rho_m}{\rho_m - \rho_c} \frac{H}{2} \right)$
F_{int}	Integrated strength of the foreland crustal column	
g	Gravitational acceleration	
h	surface elevation	
H	Orogen height, corresponds to maximum mean elevation	
h_0	Predicted maximum crustal thickness	$h_0 = h_{dec} \rho' (\sqrt{\frac{4}{Ar} + 1} - 1)$
h_{dec}	Crustal thickness above decoupling horizon	
h_{max}	maximum orogen elevation	
h_R	Rheologically controlled maximum orogen height	$h_R \approx 5.1\,\mathrm{km}$ for normal crust; $h_R \approx 3.8\,\mathrm{km}$ for "weak" crust
P_O	Overpressure	
ρ_c	Crustal density	$\rho_c = 2750\,\mathrm{kg/m^3}$
ρ_m	Mantle density	$\rho_m = 3250\,\mathrm{kg/m^3}$
ρ'	Isostatic compensation factor	$\rho' = 1 - \frac{\rho_c}{\rho_m} \approx 0.15$
τ_{xx}	horizontal deviatoric stress	
U	Uplift rate	
U_{max}	Maximum average uplift rate	$U_{max} = \frac{v_c \cdot h_{dec}}{W}$
v_c	Convergence velocity	
W	Orogen width	
W_{min}	Minimum orogen width during growth phase II	$W_{min} \approx 80\,\mathrm{km}$
$\dot{W}$	Orogen widening rate	
$\dot{W}_0$	Orogen widening rate without surface processes	
Related to surface processes		
A	Drainage area	
b, k	Hack's law exponents	$A = kx^b$; $k \approx 0.5, b \approx 2$
G	Deposition coefficient	
h_{sst}	Maximum steady-state river elevation	
K_f	Fluvial erodibility	
K_f'	Fluvial erodibility of classic stream power law without G	$K_f' = \frac{K_f}{(1+G)}$
L	River length	$L \approx \frac{W}{2}$
m, n	Stream power law exponents	
N_e	Uplift-erosion number	$N_e = \frac{0.5^{bm-n} K_f k^m {W_{min}}^{bm-n+1} H_0^n}{v_c h_{dec} (1+G)}$
S	Local slope	
τ	River response time to perturbation	
Combining (fluvial) erosion and tectonics in collisional orogens		
Bm	Beaumont number	$Bm = \frac{Ar}{N_e}$

to erosion, keeping the rheologically-controlled maximum height.

These force considerations also explain why Type 3 orogens do not form major thrusts on the pro-side, and what defines the transition from phase 1 to 2. If the orogen does not reach h_R, because its height is limited by surface processes (Type 3), the orogen also does not create the necessary gravitational potential energy variation to form pro-side thrusts, and it is energetically most favourable to form a crustal monocline. The transition from phase 1 to 2 is marked by the formation of a second thick-skinned thrust sheet. Our models show an initial 5 Myr-long phase of localisation until the initial pro-and retro-step-up shears are formed. Then, shortening creates surface uplift of the first thrust sheet until the second thrust sheet forms after ~ 10 Myr. This can be seen in the development of the buoyancy force in models 1-3 (Extended Data Fig. 2). Therefore, the timescale of phase 1 in our models is in the order of 5 Myr, and we expect the transition from phase 1 to 2 after convergence of $\Delta x \approx 50$ km of two continental plates with "normal" crustal thickness of 20 to 40 km.

4.1.2 Analytical results and relationship with Argand number

The logic that we developed from model observations can also be derived in a simple analytical relationship relating depth-integrated stresses [e.g. 26, 27]. Following the notation and derivation of Schmalholz *et al.* [27], one can show that the variation in gravitational potential energy (GPE) between orogen foreland and mountain belt is equal to the variations in depth-integrated overpressure $\bar{P}_O$ and horizontal deviatoric stress $\bar{\tau}_{xx}$:

$$F_b = \frac{\partial}{\partial x}(GPE) = \frac{\partial}{\partial x}(\bar{P}_O + \bar{\tau}_{xx}), \tag{S7}$$

where the overbar denotes depth-integrated values from the surface to the compensation depth. Hence, any difference in GPE between lowland and high mountains is related to differences in integrated tectonic overpressure and integrated horizontal deviatoric stress, $F_b = \Delta GPE = \Delta(\bar{P}_O + \bar{\tau}_{xx})$.

Using the relationship that $P_O = \tau_{xx} + Q$, where Q represents shear stresses, and utilising the thin-sheet approximation which assumes zero shear stresses, $Q = 0$ [28, 29], eq. S7 can be simplified to:

$$F_b = \frac{\partial}{\partial x}(GPE) \approx \frac{\partial}{\partial x}(2\bar{P}_O) \approx \frac{\partial}{\partial x}(2\bar{\tau}_{xx}). \tag{S8}$$

Equations S7 and S8 are valid without any assumption about the depth of compensation and geometry of the deformed lithosphere. We observe in our models that $\bar{P}_O \approx \bar{\tau}_{xx} \approx F_{int}$ and that

$$F_b \approx \bar{P}_O + \bar{\tau}_{xx} \approx 2F_{int}, \tag{S9}$$

where $\bar{P}_O$ and F_{int} are measured in the foreland crustal column (Extended Data Fig. 2). Hence, it seems that the F_b is to first order transferred to the crustal column in the orogenic

foreland. Making the simplifying, but reasonable, assumption that all orogenic topography is compensated by a crustal root, F_b can be computed as [e.g. 27]:

$$F_b = \rho_c g H \left(h_{dec} + \frac{\rho_m}{\rho_m - \rho_c} \frac{H}{2} \right) = \rho_c g H \left(h_{dec} + \frac{1}{\rho'} \frac{H}{2} \right). \tag{S10}$$

Orogen height can furthermore by approximated by

$$H = h_{dec} \rho' \left(\beta - 1 \right), \tag{S11}$$

where $\rho' = (1 - \frac{\rho_c}{\rho_m})$ is the isostatic compensation factor, which can be extended to include regional flexure [30], and β is the crustal thickening factor. Further, we can combine eq. S9, S10, and S11 to:

$$\rho_c \rho' g h_{dec}^2 \left(\frac{1}{2} \beta^2 - \frac{1}{2} \right) = 2 F_{int}. \tag{S12}$$

From eq. S12, we can define the maximum thickening factor β_0 and corresponding height h_0 at which orogens stop growing in height, and start widening:

$$\beta_0 = \sqrt{4 \frac{F_{int}}{\rho_c \rho' g h_{dec}^2} + 1} = \sqrt{\frac{4}{Ar} + 1}, \tag{S13}$$

$$h_0 = h_{dec} \rho' (\sqrt{\frac{4}{Ar} + 1} - 1), \tag{S14}$$

where Ar is the crustal Argand number. The Argand number is the ratio of excess pressure resulting from crustal thickness variations over the stress required to deform the lithosphere, and was defined by England & McKenzie [28, 29]. Ar is a non-dimensional number that can be derived from the Navier-Stokes equations [see for instance 31]. We use a similar crustal Argand number as defined by Ellis *et al.* [31], which is the ratio of the buoyancy forces from mountain building over the integrated strength of the crustal column, $Ar = \frac{\rho_c \rho' g h_{dec}^2}{F_{int}}$. The definition by Ellis *et al.* [31] is the depth-integrated version of the definition by England & McKenzie [28, 29], only applies to the crust, and represents a force ratio rather than a stress ratio.

Computing β_0 and h_0 from our models, we can compare whether the approximations from our analytical derivation agree with model behaviour. Using $F_{int} = 2.4 \times 10^{12}\,\mathrm{N/m}$ for normal crustal strength and $F_{int} = 1.5 \times 10^{12}\,\mathrm{N/m}$ for weak crust, as measured in the foreland of our models, results in $\beta_0 = 2.2$, $h_0 = 4500\,\mathrm{m}$, and $\beta_0 = 1.8$, $h_0 = 3150\,\mathrm{m}$, respectively. These values fit very well with the observed rheologically controlled maximum height for the Type 2 models in our different model sets: $h_R = 4850\,\mathrm{m}$ for MK_f5 (Extended

Data Fig. 3), $h_R = 3250\,\mathrm{m}$ for MK_f5weak (Extended Data Fig. 5). The similarity between observed and computed values supports our inference that the transition from Type 2 to Type 3 is marked by the absence of thrust sheet formation on the pro-side. However, Type 1 models with lower fluvial erodibility have consistently higher maximum mean elevation than predicted by our analytical relationships. Looking at Model 1 ($MKf05$, Fig. 1), we see that the maximum mean elevation in these kinds of models is located near the orogen boundary, and related to local "tectonic" topography of single thrust sheets. However, taking an average over several thrust sheets fits well with the analytically computed h_0. Therefore, we interpret that undeveloped fluvial relief in thrust-related, local tectonic topography explains the observed trend in Type 1 orogens that maximum mean orogen height decreases with increasing K_f.

The analytical scaling and good agreement with model observations has wide implications: a) It shows that the tectonics of mountain building in our models is to first order described by the Argand number of the crust. b) Assuming that our models are a reasonable representation of mountain belts on Earth, our derivation indicates that the Argand number is possibly the key non-dimensional number to describe collisional mountain belts on Earth. c) It shows that we can use eq. S14 to approximate the Argand number, and therefore crustal strength of any orogen composed of several crustal-scale thrust sheets, thus wider than $W_{min} = 80 - 90\,\mathrm{km}$, and which therefore has reached h_R.

4.2 The physics of fluvial surface processes - Damköhler numbers of fluvial surface processes systems

In most general terms, fluvial surface surface processes can be cast into a production-reaction-diffusion-advection problem and therefore described by a set of non-dimensional Surface Processes Damköhler numbers Da_{SP}. The primary purpose of defining the Damköhler Numbers is to provide a general framework that relates mass fluxes among landscape surface processes. Particular surface processes models, like the stream power model used here, can then be cast in terms of this framework while retaining the role of the Damköhler Numbers as the primary controls on the system.

Consider an idealistic "box model" for surface processes in which transport is described as fluxes between a set of reservoirs (R_i, see Extended Data Fig. 8). Tectonic plate movement or isostatic uplift provides an uplift flux into R_1, the uplifted intact substrate reservoir (Earth's crust). Hillslope diffusion (Qd) transports mass flux from the intact substrate (R_1) to the transportable mass reservoir R_2. This mass flux could also include an intermediate reservoir if regolith-formation is considered. Fluvial erosion through abrasion and other processes is a reaction that also converts R_1 to R_2, with a mass flux Qr. Fluvial transport by the river system advects mass flux Qa_1 from the transportable mass reservoir R_2 to R_3, the fluvially transported mass reservoir. Downstream the inverse can occur, when mass flux Qa_2

is deposited and goes from R_3 to R_2.

The system is characterized by the mass fluxes Qu, Qr, Qd, Qa or equivalently by the rates at which these fluxes are generated. The relative efficiencies of processes can be described by a set of Surface Processes Damköhler numbers Da_{SP}:

$$Da_{SP}I = \frac{Qr}{Qa} \tag{S15}$$

$$Da_{SP}II = \frac{Qr}{Qd} \tag{S16}$$

$$Da_{SP}III = \frac{Qa}{Qd} \tag{S17}$$

$$Da_{SP}IV = \frac{Qa}{Qu} \tag{S18}$$

We can see that the Da's can be defined at a local scale and globally, and more ratios can be defined that are useful under certain circumstances. $Da_{SP}I$ controls the mass flux out of an orogen, where Qa needs to take into account advection ($Qa1$) and deposition ($Qa2$). $Da_{SP}II$ determines the locally dominant erosion process, and $Da_{SP}III$ determines out-flux of mass in diffusion-dominated systems. Note that $Da_{SP}III$ is the Peclet number of the surface processes system. $Da_{SP}IV$ is the most useful number in the context of uplift versus erosion and the relative efficiency of denudation at the orogen scale, as it is defined as the ratio of mass in- and out-flux.

We can now see how the (extended) Stream Power Law (SPL) operates (eq. S6). The SPL does not consider R2, and the Qr is immediately converted to Qa, as there is no specific transport capacity. Hence, $Da_{SP}I = 1$ in the SPL, and 'erosion' means both reaction and advection. The Stream Power model has the advantage of having been widely used, as for instance in this study, but has a disadvantage that reaction and advection are conflated together. This might also explain why only one K_f factor exists and why it has such a large range of values. In the more general case there would be a K_r, the reaction coefficient, and a K_a, the advective transport coefficient. $Da_{SP}IV$ of the SPL is equivalent to the uplift-erosion number N_e, the critical non-dimensional number determining the behaviour of the SPL [32].

Following the derivation of Whipple & Tucker [32], the classic stream power law without the depositional G-term [4, 33], can be non-dimensionalized to:

$$\frac{\partial h*}{\partial t*} = U* - N_e \, x*^{bm} \, \frac{\partial h*}{\partial x*}^{n}, \tag{S19}$$

with $h* = \frac{h}{H_0}$, $x* = \frac{x}{L_0}$, $U* = \frac{U}{U_0}$, $t* = \frac{tU_0}{H_0}$, where H_0, L_0, U_0 are representative height, length, and uplift scales, respectively, and N_e is the uplift-erosion number

$$N_e = \frac{K'_f k^m L_0^{bm-n} H_0^n}{U_0}, \tag{S20}$$

where K'_f is the fluvial erodibility, and the asterix denotes non-dimensional variables. High N_e means very efficient surface processes, low N_e implies low surface process efficiency. Note that we use the inverse of Whipple & Tucker [32]'s uplift-erosion number. The inverse follows the convention of Willett [34], who also defined a similar, but simpler, uplift-erosion number.

Yuan *et al.* [4] show that the effects of sediment deposition modelled by the G-term in eq. S6, can be included in the stream-power coefficient K'_f by redefining $K'_f = \frac{K_f}{(1+G)}$. Furthermore, choosing meaningful values for the scaling parameters $L_0 = \frac{W_{min}}{2}$, $U_0 = U_{max@W_{min}} = \frac{v_c h_{dec}}{W_{min}}$, remembering that v_c should be considered as the horizontal convergence velocity that results in thickening-induced uplift U, gives

$$N_e = \frac{0.5^{bm-n} K_f k^m {W_{min}}^{bm-n+1} H_0^n}{v_c h_{dec}(1+G)}. \tag{S21}$$

This derivation shows the particular functional form of $Da_{SP}IV$ in the (extended) Stream Power Law and highlights the applicability of the Surface Processes Damköhler numbers.

4.3 Scaling surface processes and tectonics during orogenic growth

We define a new non-dimensional number, termed Beaumont-number Bm, that captures the interaction between surface processes and tectonics. We propose the name Beaumont-number, as Beaumont *et al.* [25], and Chris Beaumont and his group during the following years, were the first to develop coupled tectonic-surface process models similar to ours, and used them to investigate the feedbacks between tectonics, surface processes, and ultimately climate. Bm is defined as the ratio between the essential non-dimensional number describing tectonics, N_{Tec}, and the essential non-dimensional Surface Processes Damköhler number determining surface processes efficiency:

$$Bm = \frac{N_{Tec}}{Da_{SP}}. \tag{S22}$$

For mountain belts growing by crustal thickening, we derived above that the Argand number Ar of the continental crust is the key non-dimensional number [28, 29, 31]:

$$Ar = \frac{\rho_c g \rho' h_{dec}^2}{F_{int}}. \tag{S23}$$

$Da_{SP}IV$ is the important non-dimensional number determining mass in- and out-flux in systems dominated by fluvial surface processes, so that

$$Bm = \frac{Ar}{Da_{SP}IV} \tag{S24}$$

is the Beaumont number that captures the interaction between surface processes and tectonics in actively growing mountain belts. Large Bm imply inefficient surface processes, which results in Type 1 orogens, and low Bm mean that surface processes are efficiently counteracting orogenic growth, which results in Type 3 orogens

Specifically, in case surface processes are determined by the (extended) Stream Power Law, as in our models, $Da_{SP}IV$ is represented by the uplift-erosion number N_e, and

$$Bm = \frac{Ar}{N_e}, \tag{S25}$$

$$Bm = \frac{\rho_c g \rho' h_{dec}^3 v_c (1+G)}{0.5^{bm-n} K_f k^m W_{min}^{bm-n+1} H_0^n F_{int}}. \tag{S26}$$

Defining $H_0 = h_{dec}\rho'$ as a typical height scale, using $b \approx 2$ and $k \approx 0.5$, and employing $n = 1, m = 0.4$, as used in our models, simplifies eq. S26 to:

$$Bm = \frac{\rho_c g h_{dec}^2 v_c (1+G)}{0.5^{0.2} K_f W_{min}^{0.8} F_{int}}. \tag{S27}$$

4.4 Beaumont number of modelled orogens

We use the model sets with normal crustal strength, and weak crust, and ran a new model set with half the convergence velocity ($v_c = 0.5\,\mathrm{cm/yr}$) and variable K_f. Measuring F_{int} in the foreland crustal column, $F_{int} = 2.3 \times 10^{12}\,\mathrm{N\,m^{-1}}$ (normal crust models), $F_{int} = 1.5 \times 10^{12}\,\mathrm{N\,m^{-1}}$ (weak crust models), $F_{int} = 2.1 \times 10^{12}\,\mathrm{N\,m^{-1}}$ (slow convergence rate models), and using $\rho_c = 2750\,\mathrm{kg\,m^{-3}}$, $h_{dec} = 25\,\mathrm{km}$, $G = 1$, $W_{min} = 80\,\mathrm{km}$, $v_c = 1\,\mathrm{cm/yr}$ or $v_c = 0.5\,\mathrm{cm/yr}$, we can compute Bm of each modelled orogen. Unique for each Type 1 orogen is its widening rate ($\dot{W}$) as a function of fluvial erodibility, while orogen height is relatively independent on surface processes efficiency, $H \approx h_R$. In contrast, unique for each Type 3 orogen is its height-dependence on K_f, and constant orogen width ($\dot{W} = 0$). Therefore, plotting the normalised widening rate ($\frac{\dot{W}}{\dot{W}_0}$) and normalised height ($\frac{H}{h_R}$) versus the Beaumont number, provides a way to visualise the effects of variable Bm and allows for comparison with Nature (Fig. 3). $\dot{W}_0$ is the widening rate without surface processes, H is the average maximum mean elevation during phase 2 of model development of each model, and h_R is the average rheologically controlled height per model set. $h_R = 5100\,\mathrm{m}$ for normal crust, $h_R = 3700\,\mathrm{m}$ for weak crust, $h_R = 4600\,\mathrm{m}$ for slow convergence velocity. Furthermore, additional models without surface processes show that $\dot{W}_0 = 8.1\,\mathrm{km/Myr}$ for normal crust, $\dot{W}_0 = 9.8\,\mathrm{km/Myr}$ for weak crust, $\dot{W}_0 = 4.8\,\mathrm{km/Myr}$ for halved convergence velocity and normal crustal strength. Note also that the widening rate, $\dot{W}$, should be regarded as the rate at which the orogen increases its horizontal extent, whether it is by constant lengthening as predicted by our 2D models, or by a more complex non-uniform or lateral widening.

Supplementary Table 3 | Bm parameters related to models shown in Fig. 3a. One representative F_{int} and h_R is chosen per model set. See supplementary Table 2 for parameter definitions.

Bm (-)	K_f ($\times 10^{-5}$ m$^{0.2}$/yr)	v_c (cm/yr)	F_{int} ($\times 10^{12}$ N/m)	H (m)	h_R (m)	$\dot{W}$ (km/Myr)	$\dot{W}_0$ (km/Myr)
Reference models							
3.86	0.5	1	2.4	6240	5100	8.1	8.1
1.93	1	1	2.4	5460	5100	6.7	8.1
0.96	2	1	2.4	5370	5100	2.9	8.1
0.64	3	1	2.4	4810	5100	0.9	8.1
0.39	5	1	2.4	4610	5100	≈ 0	8.1
0.28	7	1	2.4	3880	5100	≈ 0	8.1
0.19	10	1	2.4	2780	5100	≈ 0	8.1
0.10	20	1	2.4	1710	5100	≈ 0	8.1
0.04	50	1	2.4	680	5100	≈ 0	8.1
Weak crust models							
6.17	0.5	1	1.5	4660	3700	9.8	9.8
1.03	3	1	1.5	3130	3700	2.5	9.8
0.62	5	1	1.5	3100	3700	0.8	9.8
0.44	7	1	1.5	3340	3700	≈ 0	9.8
0.31	10	1	1.5	2680	3700	≈ 0	9.8
0.15	20	1	1.5	1500	3700	≈ 0	9.8
0.06	50	1	1.5	620	3700	≈ 0	9.8
Slow convergence rate models							
2.21	0.5	0.5	2.1	5240	4600	4.2	4.8
1.23	0.9	0.5	2.1	4560	4600	2.5	4.8
0.55	2	0.5	2.1	4810	4600	0.8	4.8
0.22	5	0.5	2.1	3100	4600	≈ 0	4.8
0.11	10	0.5	2.1	1790	4600	≈ 0	4.8

Looking at Fig. 3, we see that all three model sets develop into a similar pattern: Orogens with $Bm < 0.5$ reach flux steady state. These are characterised by a decrease in $\frac{H}{h_R}$ with decreasing Bm, and $\frac{\dot{W}}{\dot{W}_0} \approx 0$. Orogens with $Bm > 0.5$ do not reach flux steady state, show increasing $\frac{\dot{W}}{\dot{W}_0}$ with increasing Bm, and have $\frac{H}{h_R} \approx 1$. Type 2 orogens, those which reach steady state but also h_R, mark the transition to non-flux steady state and have $Bm \approx [0.4 - 0.5]$. Furthermore, we see that orogens with large $Bm > 4$ have the same widening rates as orogens without surface processes. This is for instance the case in model 1, which has underfilled foreland basins that are successively integrated into the mountain belt during thick-skinned thrusting, preventing net mass loss.

4.5 Steady-state elevation and response time of fluvial landscapes

Assuming uniform K_f, n, m, G, a river length L, applying Hack's law, and given a uniform uplift rate, we can compute the steady state river long profile, its maximum elevation h_{sst},

and its response time to perturbation τ [4, 32]:

$$\tau = \frac{h_{sst}}{U} = (1+G)^{\frac{1}{n}} U^{\frac{1}{n}-1} K_f^{-\frac{1}{n}} k^{-\frac{m}{n}} \left(1 - b\frac{m}{n}\right)^{-1} L^{1-b\frac{m}{n}}, \text{ for } bm \neq n \tag{S28}$$

$$h_{sst} = \tau \cdot U. \tag{S29}$$

where G, m, n, and K_f are variables from the (extended) stream power model, L is the length of the river profile, and k and b are Hack's law coefficients [$A = kL^b$; 35], usually close to 0.5 and 2, respectively. The corresponding equation for $bm = n$ is omitted, as we use $b = 2$, $\frac{m}{n} = 0.4$ throughout the manuscript. τ is relatively insensitive to the length of the river profile, as L only has a weak influence with $L^{0.2}$, given $\frac{m}{n} = 0.4$. Our models indicate that rivers flow predominantly in transverse valleys in steady state orogens. Therefore, we make the simplifying assumption that river length equals to half the orogen width $L = W/2$.

As discussed above, G, m, n, K_f, L, k, and b are relatively well known, but the fluvial erodibility K_f, and uplift U are poorly constrained. In case of flux steady state, erosion fully balances the tectonic material influx, and the average erosion rate is equal to the maximum average surface uplift rate:

$$U_{max} = \frac{v_c \cdot h_{dec}}{W}, \tag{S30}$$

where v_c is convergence velocity, h_{dec} is the crustal decoupling level, and W is orogen width. Simplifying $U = \bar{U}_{max}$, we can substitute eq. S30 into eq. S29, and express the steady state river elevation h_{sst} as a function of plate velocity, crustal decoupling depth, and orogen width:

$$h_{sst} = (1+G)^{\frac{1}{n}} \left(\frac{v_c h_{dec}}{W}\right)^{\frac{1}{n}} K_f^{-\frac{1}{n}} k^{-\frac{m}{n}} \left(1 - b\frac{m}{n}\right)^{-1} \left(\frac{W}{2}\right)^{1-b\frac{m}{n}}, \text{ for } bm \neq n. \tag{S31}$$

Inversely, knowing the maximum height h_{sst} and width of a mountain belt at flux steady state, we can use eq. S31 to compute its fluvial erodibility:

$$K_f = (1+G) \left(\frac{v_c h_{dec}}{W}\right) k^{-m} \left(1 - b\frac{m}{n}\right)^{-n} \left(\frac{W}{2}\right)^{n-bm} h_{sst}^{-n}, \text{ for } bm \neq n. \tag{S32}$$

5 Comparison to Natural Examples

With the given set of equations and relationships, we can position real collisional orogens on Earth into the Bm-plot and get information about their crustal strength, and average fluvial erodibility. For a Type 1 orogen, we can use orogen height and eq. S14 to get its Argand number and thereby also crustal strength. Furthermore, knowing $\frac{\dot{W}}{\dot{W}_0}$ during phase-2-growth,

we can position the orogen in the Bm-plot, infer its approximate Bm-number and therewith gain information about its average K_f using eq. S27. Positioning Type 2 orogens is simpler, as we can compute crustal strength and Argand number from orogen height, and K_f with eq. S32. Positioning Type 3 orogens in the Bm-plot is more difficult as h_R is unknown. Assuming bounds on h_R, or making an approximation of h_R based on convergence rate, thermal state, and composition, allows rough positioning of these orogens in the Bm-plot as well.

In the following, we give an extensive supplementary comparison to the Southern Alps of New Zealand (SANZ), Taiwan, Himalaya-Tibet, and the Central Andes. The Andes and Taiwan do not form in a continent-continent collision system as shown in the models here, but during arc-continent collision or ocean-continent subduction, respectively. However, both orogens form to first order as a consequence of crustal thickening and independent evolution of crust and mantle. Hence, their dynamics is most likely also determined by the crustal Argand number, which makes them suitable to compare to our developed scaling analysis. As seen below, the central and southern Andes even show the different stages of orogenic growth portrayed in Fig. 4.

5.1 Southern Alps of New Zealand

The Southern Alps of New Zealand (SANZ) are an active mountain belt forming through continent-continent collision of the Pacific (pro-) and the Australian (retro-) plate (Extended Data Fig. 10a). Convergence has a large right-lateral strike-slip component of 30 to 40 mm/yr, and a normal component of 8 to 10 mm/yr [36]. Crustal shortening is largely accommodated by thrusting on the Alpine fault, which brings upper- to middle-crustal rocks in its hanging wall to the surface. These rocks are metamorphosed and strongly deformed near the fault zone [Extended Data Fig. 10a, e.g. 20, 37–39]. The hanging wall contains a series of NW-dipping reverse faults that accommodate little thrust motion compared to the main Alpine fault [21, 38]. The crustal décollement level is generally inferred to be at 25 to 30 km depth [39, 40], and shortening in its current regime started at around (10 to) 5 Ma, with convergence estimates between 50 and 80 km [37]. Rise of the Southern Alps obstructed the predominantly westerly winds, which changed climate at around 5 Ma and created a strong partitioning of precipitation between a very wet W and drier E side of the orogen [41]. During glacial periods of the Quaternary, the Southern Alps were furthermore widely covered by ice on both mountain flanks [42]. Glaciations and high precipitation rates are generally attributed as cause for extremely high erosion and exhumation rates, reaching > 5 mm/yr [34, 43, 44]. Today the orogen is 80 to 110 km wide and has a maximum mean elevation of only $1.8 - 2$ km, and an absolute maximum elevation of around 3 km (Extended Data Fig. 10a).

The monoclinal orogenic structure with one major retro-shear zone and no significant pro-

side thrusting, very high exhumation rates in the order of the plate convergence rate, small orogen width, primarily transverse valleys, and low maximum mean elevation indicate that the Southern Alps of New Zealand are a prime example of a Type 3 orogen. Since $W = W_{min}$, we can use eq. S32 to calculate K_f, assuming that the stream power law governs orogen height, and that erosion follows the same stream power law parameters as used in our set of models (i.e. $m = 0.4$, $n = 1$, etc.). Using an average depth to the crustal detachment horizon, $h_{dec} \approx 25\,\mathrm{km}$, and $v_c \approx 1\,\mathrm{cm/yr}$ (Extended Data Fig. 10a) results in $K_f \approx 11 \times 10^{-5}\,\mathrm{m}^{0.2}/\mathrm{yr}$. Given that the Earth-absolute limit for maximum $h_R \approx 5\,\mathrm{km}$, $2\,\mathrm{km} < h_R < 5\,\mathrm{km}$, using eq. S14 and eq. S11, we can limit $0.85 \times 10^{12}\,\mathrm{N/m} < F_{int} < 2.78 \times 10^{12}\,\mathrm{N/m}$. With these limits we can compute $0.15 < Bm < 0.48$ and plot the Southern Alps of New Zealand into Fig. 3.

5.2 Taiwan

Taiwan is an actively growing mountain belt that started forming at 5 to 7 Ma through collision between the South China Sea passive margin of the European plate (pro-side), and the Luzon arc of the Philippine Sea plate (retro-side). The oblique collision with convergence rate of $\sim 8.0\,\mathrm{cm/yr}$ [$\sim 7.2\,\mathrm{cm/yr}$ normal component; 45] results in southward propagation of shortening at a rate of 31 to 60 mm/yr [46, 47]. This time-space transformation relates younger growth stages in the S to more mature orogen structure in the centre. The central part of the orogen has furthermore a constant width of 80 to 100 km. The N-part of Taiwan is affected by extension, related to back-arc spreading behind the Ryukyu arc [48]. Structurally, Taiwan forms by inversion of the South China Sea passive margin, which creates a forward breaking foreland fold-thrust belt, antiformal duplexing in the orogen centre, and inverts extensional faults [18, 19, 49–51]. Shortening involves primarily the Eurasian plate, which has a thickness of $\sim 30\,\mathrm{km}$, and a mafic lower crust, resulting in $h_{dec} \approx 20\,\mathrm{km}$ [Extended Data Fig. 10b; 19]. Taiwan's tropical climate with seasonal typhoons and high deformation rates lead to extremely high erosion and exhumation rates [51, 52]. The extremely high erosion rates and relatively constant orogen width in the centre show that Taiwan possibly reached flux steady state [53]. River topology is dominated by transverse valleys, which supports flux steady state. However, the central W-flank shows some longitudinal flow in the orogen centre. Furthermore, Fox *et al.* [54] argue that current rock uplift rates exceed erosion rates in many parts of the orogen. River topology, erosion rates, constant orogen width, and orogen structure indicate that Taiwan is possibly right at the boundary between a flux steady state and a non-steady state orogen, and therefore possibly an example of a Type 2 orogen.

Using eq. S32, $h_{max} = 4 \times 10^3\,\mathrm{m}$, $H = h_R = 2.8\,\mathrm{km}$, $h_{dec} = 20\,\mathrm{km}$, $v_c = 7.2\,\mathrm{cm/yr}$, and the parameters of the stream-power law as used in our models, we obtain $K_f \approx 47 \times 10^{-5}\,\mathrm{m}^{0.2}/\mathrm{yr}$. Using eq. S14 and eq. S11, we can calculate $F_{int} \approx 1.1 \times 10^{12}\,\mathrm{N/m}$ and $Bm \approx 0.4$. F_{int} is lower than in our models. Low F_{int} fits well with weak extensional struc-

tures that form the foreland of mountain belt in Taiwan. The extremely high K_f also fits well with the high, typhoon driven erosion rates [52].

5.3 Himalaya-Tibet

Himalaya-Tibet is an actively growing orogen that formed in its current configuration by the collision between India and Eurasia which started around 59 Ma [17, 55, 56]. Current plate convergence rates are $v_c \approx 4.5\,\mathrm{cm/yr}$, but were significantly higher in the past, resulting in 4000 km of plate convergence since 58 Ma, and average convergence rate $v_c =\sim 6.9\,\mathrm{cm/yr}$ [57, 58]. Collision formed a very large orogen with a central plateau (Extended Data Fig. 10c), and there is evidence that India collided with already pre-thickened Tibetan crust [59–62]. The orogen sits largely on the retro-side (Extended Data Fig. 10c), which can possibly be explained by collision with pre-thickened crust, or initiation of shortening in the Qiangtang terrane [58, 63], and enhanced erosion at the wet Himalayan mountain front [64, 65]. The crustal decoupling level in the Indian plate is at depth of $h_{dec} = 19 - 28\,\mathrm{km}$ [16, 17, 57], leading to significant continental subduction of likely mafic lower crust [57]. Ingalls *et al.* [57] infer that $\sim 465 \pm 185 \times 10^3\,\mathrm{Gt}$ of crustal mass were involved in formation of the Himalaya-Tibet orogen, whereof $140 \pm 28 \times 10^3\,\mathrm{Gt}$ are eroded. Using respective maximum and minimum values, this means that at most 60 % and at least 17 % of the orogen were eroded during growth, giving $\frac{\dot{W}}{\dot{W}_0} = 61.5 \pm 21.5\,\%$. The Himalayas are the highest and widest orogen on Earth, with maximum average elevation of $H = 5.0 \pm 0.5\,\mathrm{km}$ (Extended Data Fig. 10c), and width of $\sim 520\,\mathrm{km}$ in the West and $\sim 1300\,\mathrm{km}$ in the East.

Following eqs. S11 and S14, assuming an average $h_{dec} = 24\,\mathrm{km}$ and typical values for crust and mantle densities (Table 3), $H = 5.0 \pm 0.5\,\mathrm{km}$ results in a crustal thickening factor $\beta_0 = 2.34 \pm 0.13$, crustal $Ar = 0.88 \pm 0.13$, and crustal integrated strength of $F_{int} = 2.7 \pm 0.4 \times 10^{12}\,\mathrm{N/m}$. Placing the Himalayan-Tibetan orogen in the Bm-plot, we find that this particular orogen has a $Bm \approx 1.5 \pm 0.5$. Knowing Bm, we can approximate the orogen average $K_f = 4.7 - 12.5 \times 10^{-5}\,\mathrm{m^{0.2}/yr}$, with mean $K_f = 7.2 \times 10^{-5}\,\mathrm{m^{0.2}/yr}$. We note, however, that this result is heavily dependent on $\frac{\dot{W}}{\dot{W}_0}$ and the resulting positioning in the Bm-plot. Replumaz *et al.* [17], for instance, argue that only 15 % of the Indian crust and 2 % of the Tibetan crust are eroded. Including that $40 - 50\,\%$ of the Indian crust are subducted, and that the Indian crust builds 1/4 of the orogen, gives a rough estimate that only 8 % of the crust involved in the orogeny is eroded, and thus $\frac{\dot{W}}{\dot{W}_0} = 0.92$. This is much lower than the values from Ingalls *et al.* [57] and relates to different sedimentary mass budgets taken into account in both studies. $\frac{\dot{W}}{\dot{W}_0} = 0.92$ indicates $Bm \approx 3$ (Fig. 3), which leads to $K_f \approx 3.6 \times 10^{-5}\,\mathrm{m^{0.2}/yr}$, using average F_{int}.

The Himalayas constitute a strong precipitation barrier, with a very wet mountain front and a dry central plateau. Given that we calculated mountain-wide and time-averaged K_f

values $> 5 \times 10^{-5}\,\mathrm{m}^{0.2}/\mathrm{yr}$, the fluvial erodibility in the frontal Himalayas must be extremely high, possibly up to one magnitude higher than the mountain belt average. High K_f in the mountain front fit with modelling studies that showed that orogenic structure of the Himalayas can in part be explained by focussed and high erosion rates at the Himalayan mountain front [e.g. 66]. Computed integrated strength of the Indian crust $F_{int} = 2.7 \pm 0.4 \times 10^{12}\,\mathrm{N/m}$ fits well with height and integrated strength of our modelled orogens, and independent stress estimates [e.g., 27].

5.4 Central Andes

The cental part of the Andes is actively growing and forms by crustal thickening with up to several hundreds of km of crustal shortening of the South American plate in an ocean-continent subduction setting [67, 68]. Decoupled evolution of crust and mantle, and orogen formation related to crustal thickening allows a simple first order comparison of the Andes to the Bm number developed here despite the Andes forming during ocean-continent subduction and not during continent-continent collision. The Andes have an ubiquitous pre-collisional extension history [e.g. 69–71], where phases of back-extension and shortening can be attributed to absolute plate velocity changes [2, 72, 73]. The main, current shortening phase started around 50 Ma and deformation propagated from the West to the East [68, 72, 74]. Orogen-wide convergence rate v_c is a function of the trench-normal plate velocity minus the trench retreat velocity [2, 75, 76]. Currently the highest convergence rates ($v_c \approx 1 \pm 0.5\,\mathrm{cm/yr}$) are found in the orogen centre that also forms an orogenic plateau [75, 76]. Convergence rates decrease towards the South and North, and the northern- and southernmost parts exhibit a neutral overriding plate strain regime [75, 76].

Looking at the area between the plateau-like central Andes and the southernmost Andes, we observe that the Andes South of around 38° have a high trench retreat velocity and are currently not shortening, while the part North of around 38° S is actively shortening [absolute plate velocity maps of 75, 76]. Additionally, we observe that north of circa 38° S, the orogen consistently reaches maximum average elevations of 4.3 to 4.6 km (Extended Data Fig. 10d), although the mountain width increases northward. Similar relationships can be shown for the northern Andes. Similar height along strike indicates that the rheology of the South American plate is relatively uniform, and supports model inferences that orogens are expected to first grow in height, then in width. We note that the trend could either be interpreted as showing a change in climate, or along-strike variability in plate convergence. However, in both cases the Central and Southern Andes are rheology-limited North of 38° S.

Crustal thickness in the central Andean foreland is in the order of 30 to 40 km [77], with variable decoupling levels creating thin- and thick-skinned deformation [e.g. 70, 72, 74]. Assuming a decoupling depth similar to the other natural examples $h_{dec} = 25\,\mathrm{km}$, typical

values for crust and mantle densities (Table 3), and using $H = 4.4 \pm 0.2\,\mathrm{km}$ results in a crustal thickening factor $\beta_0 = 2.14 \pm 0.6$, crustal $Ar = 1.11 \pm 0.07$, and crustal integrated strength of $F_{int} = 2.3 \pm 0.2 \times 10^{12}\,\mathrm{N/m}$. Because of the lack of a whole-orogen mass budges, we can only assume bounds on $\frac{\dot{W}}{\dot{W}_0}$ and hence on Bm. The central Andes have a very dry Eastern flank and wet Western side, yet do not show high exhumation rates on either orogen flank. Exhumation and the efficiency of surface processes are furthermore likely also less than in highly erosive frontal Himalayas. Hence, we assume a minimum Bm equal to the maximum Bm of Himalaya-Tibet, and $Bm < 4$ as an upper bound. These parameters give $0.5 \times 10^{-5}\,\mathrm{m^{0.2}/yr} < K_f < 1 \times 10^{-5}\,\mathrm{m^{0.2}/yr}$ for the central Andes. We note that our first order comparison does not account for local anomalies in topography, likely related to anomalous thermal gradients or density distributions [78].

5.5 River topology as indicator for (non-)steady state

Models and force considerations also explain why thrust-induced diversion of river flow into longitudinal valleys in the core of the orogen is indicative for non-steady state growth: It is well known that if a new outward-propagating shortening feature forms, the balance between a) upstream sediment aggradation rate and incision rate through the emerging structure, and b) differential uplift rate of the emerging structure, determine whether the stream diverts its course into a longitudinal valley [79–83]. With our models we can show that if aggradation and incision are less effective than uplift, the emerging structure will grow until it reaches h_R. Consequently, a new outward-propagating thrust sheet forms, possibly forming another longitudinal valley, and the orogen grows. Hence there is a link between non-steady state growth and longitudinal valleys. Furthermore, based on our modelling results the inverse seems true, that primarily transverse valleys are an indicator for flux steady state. However, if thrusting would be different and create uniform block uplift of the whole thrust sheet, rivers would not be deflected into longitudinal valleys, although surface processes might be less effective than tectonics. Therefore, the inverse, that transverse valleys in the orogen core demonstrate flux steady state, is not necessarily true, but rather an indicator. Furthermore, not all thrusts have a thick-skinned style and create surface uplift that reaches h_R. Indeed, we observe that thin-skinned thrusts might divert river flow at the orogen boundaries even if the orogen is in flux steady state (Extended Data Fig. 6), but these longitudinal valleys related to thin-skinned thrusts are removed once they are translated towards the centre of the orogen. Summarizing, based on model results, force considerations, and comparison with previous studies, it seems reasonable that river flow in pre-dominantly longitudinal valleys in the orogen core is indicative for non-flux steady state.

6 Deriving a scaling relationship for orogenic decay

6.1 The isostatic response to erosion

Stopping plate movement ceases the tectonic flux of material and thus the tectonic surface uplift of the orogen. Instead, the uplift rate is an isostatic response to erosion and can be expressed as:

$$U = (1 - \rho') \cdot \dot{e}, \tag{S33}$$

where $1 - \rho'$ is the amount of isostatic rebound per unit erosion. For the simple case of local isostasy, $\rho' = \rho'_{local}$ can be expressed as

$$\rho'_{local} = 1 - \frac{\rho_c}{\rho_m}. \tag{S34}$$

ρ_c is the average crustal and ρ_m the average lithospheric mantle density. Regional isostatic rebound can be included into ρ' by considering the finite flexural strength of the lithosphere [30, 84]:

$$\rho'_{regional} = 1 - \frac{\rho_c}{\rho_m + \frac{D}{g}\left(\frac{\pi}{l}\right)^4}, \tag{S35}$$

where D is the flexural rigidity of the lithosphere, g is gravitational acceleration and l is the length of the eroding system. D is a function of the Young's modulus E, the effective elastic thickness T_e, and the Poisson's ratio ν:

$$D = \frac{ET_e^3}{12\left(1 - \nu^2\right)}. \tag{S36}$$

These relationships show that if variations in the erosion signal are in the order of or lower than T_e, the uplift-response to erosion, $\rho'_{regional}$, will be wider and have a lower amplitude than the erosion signal. On the contrary, if the wavelength of the erosion signal is much wider than the effective elastic thickness of the orogen, $l >> T_e$, the uplift response is virtually local isostatic, $\rho'_{regional}$ simplifies to ρ'_{local}, and the uplift and erosion signals are congruent in shape.

Through our modelling we show that orogenic decay is a two-stage process: Once convergence stops, tectonic topography with wavelength shorter than the regional isostatic rebound signal is removed quickly in a first decay phase. Slow and long-term decay of topography in phase two is characterised by effectively local-isostatic rebound. Hence, $\rho'_{regional}$ describes behavior in decay-phase 1, while ρ'_{local} describes decay-phase 2.

It is not straight forward to relate continental layered rheology to an effective elastic plate thickness T_e, as flexural strength depends not only on the relative contributions of the variable-strength layers, but also for instance on the degree of viscous coupling between the layers, and type of (un-)loading [30, 85, 86]. However, looking at the uplift signals of our

models and using the approximate estimate of $T_e = \sqrt[3]{h_{lm}^3 + h_c^3}$ [85], where h_{lm} and h_c are lithospheric mantle respectively crustal thicknesses, we find that our models have an inherent T_e of around 30 - 60 km.

6.2 Timescales of orogenic decay

Given the above relationships for the uplift rate, the change of topography of a decaying orogen can be expressed as

$$\frac{dh}{dt} = U - \dot{e} = -\rho' \dot{e} = \rho' \left(-K_f A^m S^n + \frac{G}{A} \int_A \left(U - \frac{\partial h}{\partial t} \right) dA \right). \tag{S37}$$

Furthermore, including the deposition term into K_f by using the steady-state relationship $K_f' = \frac{K_f}{1+G}$ [4], we can simplify the equation to

$$\frac{dh}{dt} = -\rho' K_f' A^m S^n. \tag{S38}$$

The rate of topographic decay decreases proportionally to S^n and thus h^n. Introducing a proportionality constant k_p, and using Hack's law ($A = kL^b$), equation S38 can be expressed as

$$\frac{dh}{dt} = -\rho' K_f' k^m L^{bm} h^n k_p. \tag{S39}$$

For $n = 1$, as used in our models, the equation integrates to

$$h(t) = (h_{initial} - h_{final}) \cdot \exp\left(-\rho' K_f' k^m L^{bm} k_p t \right) + h_{final}. \tag{S40}$$

with typical mean lifetime $\lambda = (\rho' K_f' k^m L^{bm} k_p)^{-1}$, corresponding to topographic lowering of $\approx 63\,\%$. Accordingly, $90\,\%$ of topographic lowering are attained after $\lambda_{90\,\%} = -\ln(0.1)\lambda$.

To derive a suitable first-order proportionality constant k_p, we ran several FastScape-only models, with the same depth as the coupled models (200 km), variable width (125 km, 250 km, 500 km), variable height ($h_{initial}, h_{initial}/2, h_{initial}/4, h_{initial}/8$), variable K_f, and with uplift defined as $U = \rho' * \dot{e}$ (see Extended Data Fig. 7). Plotting orogenic height through time, we find that $k_p \approx (W + W^2/1500 \times 10^3\,\mathrm{m})^{-1}$ is one suitable proportionality constant that fits the orogenic decay to first order. Comparing phase-2-decay of Models 1 to 3 to the analytical scaling relationship shows good fit (Extended Data Fig. 7g).

From eq. S40 and the plots in Extended Data Fig. 7 we can see that changing the initial starting height of the decaying orogen corresponds to a shift in time on the decay curve (see also Extended Data Fig. 7h). Loosing for instance some height after shortening due to post-collisional extensional collapse is equivalent to starting further down on the decay curve.

We note that low fluvial erodibilities will lead to a relatively "flat" decay curve, because the initial height inherited from the growth phase is likely limited by rheology.

Using typical, model-derived values, we can compute λ and $\lambda_{90\,\%}$ for decay phase 2 ($\rho' = \rho_{local}$): A 250 km wide orogen gives $\lambda \approx 92\,\mathrm{Myr}, \lambda_{90\,\%} = 212\,\mathrm{Myr}$ for $K_f = 0.5 \times 10^{-5}\,\mathrm{m}^{0.2}/\mathrm{yr}$ (Model 1), $\lambda \approx 9.2\,\mathrm{Myr}, \lambda_{90\,\%} = 21.2\,\mathrm{Myr}$ for $K_f = 5 \times 10^{-5}\,\mathrm{m}^{0.2}/\mathrm{yr}$ (Model 2), and $\lambda \approx 2.3\,\mathrm{Myr}, \lambda_{90\,\%} = 5.3\,\mathrm{Myr}$ for $K_f = 20 \times 10^{-5}\,\mathrm{m}^{0.2}/\mathrm{yr}$ (Model 3). All values fit very well with decay timescales observed in our models. Using $\rho' = \rho_{regional}$ (eq. S35) we can furthermore compute typical timescales for decay-phase 1, in which short-wavelength tectonic topography is quickly removed. Using typical values for the Young's modulus and Poisson's ratio, assuming an effective elastic thickness of 30 km, and using a typical wavelength-range for topography $l = 25 - 100\,\mathrm{km}$, results in $\rho' = 0.80 - 0.99$. Accordingly, $\lambda \approx 14\,\mathrm{Myr}$ for Model 1 ($K_f = 0.5 \times 10^{-5}\,\mathrm{m}^{0.2}/\mathrm{yr}$), $\lambda \approx 1.4\,\mathrm{Myr}$ for Model 2 ($K_f = 5 \times 10^{-5}\,\mathrm{m}^{0.2}/\mathrm{yr}$), and $\lambda \approx 0.4\,\mathrm{Myr}$ for Model 3 ($K_f = 20 \times 10^{-5}\,\mathrm{m}^{0.2}/\mathrm{yr}$). Again these values fit relatively well with the observe phase-one decay timescales in the models. Although these calculations are only first order approximations, they give good information about the expected timescales of orogenic decay.

We restrict our computation to $n = 1$, as used in our models. We note that the calculations can also be done with n not equal to 1. A larger exponent of n would lead to longer decay-timescales given K_f stays unchanged during decay.

References

1. Thieulot, C. FANTOM: Two- and three-dimensional numerical modelling of creeping flows for the solution of geological problems. *Physics of the Earth and Planetary Interiors* **188,** 47–68 (2011).
2. Wolf, S. G. & Huismans, R. S. Mountain Building or Backarc Extension in Ocean-Continent Subduction Systems: A Function of Backarc Lithospheric Strength and Absolute Plate Velocities. *Journal of Geophysical Research-Solid Earth* **124,** 7461–7482 (2019).
3. Braun, J. & Willett, S. D. A very efficient O(n), implicit and parallel method to solve the stream power equation governing fluvial incision and landscape evolution. *Geomorphology* **180,** 170–179 (2013).
4. Yuan, X. P., Braun, J., Guerit, L., Rouby, D. & Cordonnier, G. A New Efficient Method to Solve the Stream Power Law Model Taking Into Account Sediment Deposition. *Journal of Geophysical Research-Earth Surface* **124,** 1346–1365 (2019).
5. Bos, B. & Spiers, C. J. Frictional-viscous flow of phyllosilicate-bearing fault rock: Microphysical model and implications for crustal strength profiles. *Journal of Geophysical Research-Solid Earth* **107** (2002).
6. Sibson, R. H. Conditions for fault-valve behaviour. *Geological Society, London, Special Publications* **54,** 15–28 (1990).
7. Huismans, R. S. & Beaumont, C. Symmetric and asymmetric lithospheric extension: Relative effects of frictional-plastic and viscous strain softening. *Journal of Geophysical Research-Solid Earth* **108** (2003).
8. Gleason, G. C. & Tullis, J. A Flow Law for Dislocation Creep of Quartz Aggregates Determined with the Molten-Salt Cell. *Tectonophysics* **247,** 1–23 (1995).
9. Mackwell, S. J., Zimmerman, M. E. & Kohlstedt, D. L. High-temperature deformation of dry diabase with application to tectonics on Venus. *Journal of Geophysical Research-Solid Earth* **103,** 975–984 (1998).
10. Karato, S. & Wu, P. Rheology of the Upper Mantle - a Synthesis. *Science* **260,** 771–778 (1993).
11. Hacker, B. R., Kelemen, P. B. & Behn, M. D. Continental Lower Crust. *Annual Review of Earth and Planetary Sciences* **43,** 167–205 (2015).
12. Pysklywec, R. N. & Beaumont, C. Intraplate tectonics: feedback between radioactive thermal weakening and crustal deformation driven by mantle lithosphere instabilities. *Earth and Planetary Science Letters* **221,** 275–292 (2004).
13. Muñoz, J. A. in *Thrust tectonics* 235–246 (Springer, 1992).
14. Schmid, S. M., Pfiffner, O. A., Froitzheim, N., Schonborn, G. & Kissling, E. Geophysical-geological transect and tectonic evolution of the Swiss-Italian Alps. *Tectonics* **15,** 1036–1064 (1996).

15. Schmid, S. M., Fugenschuh, B., Kissling, E. & Schuster, R. Tectonic map and overall architecture of the Alpine orogen. *Eclogae Geologicae Helvetiae* **97,** 93–117 (2004).

16. Gao, R. *et al.* Crustal-scale duplexing beneath the Yarlung Zangbo suture in the western Himalaya. *Nature Geoscience* **9,** 555–560 (2016).

17. Replumaz, A., Negredo, A. M., Guillot, S., van der Beek, P. & Villasenor, A. Crustal mass budget and recycling during the India/Asia collision. *Tectonophysics* **492,** 99–107 (2010).

18. Brown, D., Alvarez-Marron, J., Schimmel, M., Wu, Y. M. & Camanni, G. The structure and kinematics of the central Taiwan mountain belt derived from geological and seismicity data. *Tectonics* **31** (2012).

19. Van Avendonk, H. J. A. *et al.* Deep crustal structure of an arc-continent collision: Constraints from seismic traveltimes in central Taiwan and the Philippine Sea. *Journal of Geophysical Research-Solid Earth* **119,** 8397–8416 (2014).

20. Little, T. A. Transpressive ductile flow and oblique ramping of lower crust in a two-sided orogen: Insight from quartz grain-shape fabrics near the Alpine fault, New Zealand. *Tectonics* **23** (2004).

21. Herman, F., Cox, S. C. & Kamp, P. J. J. Low-temperature thermochronology and thermokinematic modeling of deformation, exhumation, and development of topography in the central Southern Alps, New Zealand. *Tectonics* **28** (2009).

22. Griffin, W., O'Reilly, S. Y., Ryan, C., Gaul, O. & Ionov, D. Secular variation in the composition of subcontinental lithospheric mantle: geophysical and geodynamic implications. *Structure and evolution of the Australian continent* **26,** 1–26 (1998).

23. Djomani, Y. H. P., O'Reilly, S. Y., Griffin, W. L. & Morgan, P. The density structure of subcontinental lithosphere through time. *Earth and Planetary Science Letters* **184,** 605–621 (2001).

24. Hacker, B. R. in *Subduction: Top to Bottom* (eds Bebout, G. E., Scholl, D. W., Kirby, S. H. & Platt, J. P.) 337–346 (American Geophysical Union, 1996).

25. Beaumont, C., Fullsack, P. & Hamilton, J. in *Thrust tectonics* 1–18 (Springer, 1992).

26. Molnar, P. & Lyon-Caen, H. Some simple physical aspects of the support, structure, and evolution of mountain belts. *Geol. Soc. Am. Spec. Pap.* **218,** 179–207 (1988).

27. Schmalholz, S. M., Medvedev, S., Lechmann, S. M. & Podladchikov, Y. Relationship between tectonic overpressure, deviatoric stress, driving force, isostasy and gravitational potential energy. *Geophysical Journal International* **197,** 680–696 (2014).

28. England, P. & McKenzie, D. A Thin Viscous Sheet Model for Continental Deformation. *Geophysical Journal of the Royal Astronomical Society* **70,** 295–321 (1982).

29. England, P. & McKenzie, D. Correction to - a Thin Viscous Sheet Model for Continental Deformation. *Geophysical Journal of the Royal Astronomical Society* **73,** 523–532 (1983).

30. Braun, J., Simon-Labric, T., Murray, K. E. & Reiners, P. W. Topographic relief driven by variations in surface rock density. *Nature Geoscience* **7,** 534–540 (2014).

31. Ellis, S., Fullsack, P. & Beaumont, C. Oblique Convergence of the Crust Driven by Basal Forcing - Implications for Length-Scales of Deformation and Strain Partitioning in Orogens. *Geophysical Journal International* **120,** 24–44 (1995).

32. Whipple, K. X. & Tucker, G. E. Dynamics of the stream-power river incision model: Implications for height limits of mountain ranges, landscape response timescales, and research needs. *Journal of Geophysical Research-Solid Earth* **104,** 17661–17674 (1999).

33. Guerit, L. *et al.* Fluvial landscape evolution controlled by the sediment deposition coefficient: Estimation from experimental and natural landscapes. *Geology* **47,** 853–856 (2019).

34. Willett, S. D. Orogeny and orography: The effects of erosion on the structure of mountain belts. *Journal of Geophysical Research-Solid Earth* **104,** 28957–28981 (1999).

35. Hack, J. T. *Studies of longitudinal stream profiles in Virginia and Maryland* Report 294B (1957).

36. Beavan, J., Ellis, S., Wallace, L. M. & Denys, P. in *A Continental Plate Boundary: Tectonics at South Island, New Zealand* (eds Stern, T., Okaya, D. & Davey, F.) 75–94 (2007).

37. Batt, G. E. & Braun, J. The tectonic evolution of the Southern Alps, New Zealand: insights from fully thermally coupled dynamical modelling. *Geophysical Journal International* **136,** 403–420 (1999).

38. Norris, R. J. & Cooper, A. F. Late Quaternary slip rates and slip partitioning on the Alpine Fault, New Zealand. *Journal of Structural Geology* **23,** 507–520 (2001).

39. Little, T. A., Holcombe, R. J. & Ilg, B. R. Kinematics of oblique collision and ramping inferred from microstructures and strain in middle crustal rocks, central Southern Alps, New Zealand. *Journal of Structural Geology* **24,** 219–239 (2002).

40. Little, T. A., Cox, S. C., Vry, J. K. & Batt, G. E. Variations in exhumation level and uplift rate along the obliqu-slip Alpine fault, central Southern Alps, New Zealand. *GSA Bulletin* **117,** 707–723 (2005).

41. Chamberlain, C. P., Poage, M. A., Craw, D. & Reynolds, R. C. Topographic development of the Southern Alps recorded by the isotopic composition of authigenic clay minerals, South Island, New Zealand. *Chemical Geology* **155,** 279–294 (1999).

42. Barrell, D. J. A. in *Developments in Quaternary Sciences* (eds Ehlers, J., Gibbard, P. L. & Hughes, P. D.) 1047–1064 (Elsevier, 2011).

43. Batt, G. E., Braun, J., Kohn, B. P. & McDougall, I. Thermochronological analysis of the dynamics of the Southern Alps, New Zealand. *Geological Society of America Bulletin* **112,** 250–266 (2000).

44. Jiao, R., Herman, F. & Seward, D. Late Cenozoic exhumation model of New Zealand: Impacts from tectonics and climate. *Earth-Science Reviews* **166,** 286–298 (2017).

45. Yu, S. B., Chen, H. Y. & Kuo, L. C. Velocity field of GPS stations in the Taiwan area. *Tectonophysics* **274,** 41–59 (1997).

46. Simoes, M. & Avouac, J. P. Investigating the kinematics of mountain building in Taiwan from the spatiotemporal evolution of the foreland basin and western foothills. *Journal of Geophysical Research-Solid Earth* **111** (2006).

47. Byrne, T. B. in *Geology and Geophysics of An Arc–Continent Collision* (eds Byrne, T. B. & Liu, C. S.) 55–56 (Special Paper of the Geological Society of America, Taiwan, 2002).

48. Malavieille, J. & Trullenque, G. Consequences of continental subduction on forearc basin and accretionary wedge deformation in SE Taiwan: Insights from analogue modeling. *Tectonophysics* **466,** 377–394 (2009).

49. Suppe, J. A retrodeformable cross section of northern Taiwan. *Proc. Geol. Soc. China* **23,** 46–55 (1980).

50. Brown, D. *et al.* How the structural architecture of the Eurasian continental margin affects the structure, seismicity, and topography of the south central Taiwan fold-and-thrust belt. *Tectonics* **36,** 1275–1294 (2017).

51. Simoes, M. *et al.* Mountain building in Taiwan: A thermokinematic model. *Journal of Geophysical Research-Solid Earth* **112** (2007).

52. Dadson, S. J. *et al.* Links between erosion, runoff variability and seismicity in the Taiwan orogen. *Nature* **426,** 648–651 (2003).

53. Stolar, D. B., Roe, G. H. & Willett, S. D. Controls on the patterns of topography and erosion rate in a critical orogen. *Journal of Geophysical Research-Earth Surface* **112** (2007).

54. Fox, M., Goren, L., May, D. A. & Willett, S. D. Inversion of fluvial channels for paleorock uplift rates in Taiwan. *Journal of Geophysical Research-Earth Surface* **119,** 1853–1875 (2014).

55. DeCelles, P. G., Kapp, P., Gehrels, G. E. & Ding, L. Paleocene-Eocene foreland basin evolution in the Himalaya of southern Tibet and Nepal: Implications for the age of initial India-Asia collision. *Tectonics* **33,** 824–849 (2014).

56. Hu, X. M., Garzanti, E., Moore, T. & Raffi, I. Direct stratigraphic dating of India-Asia collision onset at the Selandian (middle Paleocene, 59 +/- 1 Ma). *Geology* **43,** 859–862 (2015).

57. Ingalls, M., Rowley, D. B., Currie, B. & Colman, A. S. Large-scale subduction of continental crust implied by India-Asia mass-balance calculation. *Nature Geoscience* **9,** 848–853 (2016).

58. Kelly, S., Beaumont, C. & Butler, J. P. Inherited terrane properties explain enigmatic post-collisional Himalayan-Tibetan evolution. *Geology* **48,** 8–14 (2019).

59. Kapp, P. *et al.* Mesozoic and Cenozoic tectonic evolution of the Shiquanhe area of western Tibet. *Tectonics* **22** (2003).

60. Kapp, P., Yin, A., Harrison, T. M. & Ding, L. Cretaceous-Tertiary shortening, basin development, and volcanism in central Tibet. *Geological Society of America Bulletin* **117,** 865–878 (2005).

61. DeCelles, P. G., Robinson, D. M. & Zandt, G. Implications of shortening in the Himalayan fold-thrust belt for uplift of the Tibetan Plateau. *Tectonics* **21** (2002).

62. Kapp, P. & DeCelles, P. G. Mesozoic-Cenozoic Geological Evolution of the Himalayan-Tibetan Orogen and Working Tectonic Hypotheses. *American Journal of Science* **319,** 159–254 (2019).

63. Wang, C. S. *et al.* Outward-growth of the Tibetan Plateau during the Cenozoic: A review. *Tectonophysics* **621,** 1–43 (2014).

64. Burbank, D. W. *et al.* Bedrock incision, rock uplift and threshold hillslopes in the northwestern Himalayas. *Nature* **379,** 505–510 (1996).

65. Herman, F. *et al.* Exhumation, crustal deformation, and thermal structure of the Nepal Himalaya derived from the inversion of thermochronological and thermobarometric data and modeling of the topography. *Journal of Geophysical Research-Solid Earth* **115** (2010).

66. Beaumont, C., Jamieson, R. A., Nguyen, M. H. & Lee, B. Himalayan tectonics explained by extrusion of a low-viscosity crustal channel coupled to focused surface denudation. *Nature* **414,** 738–742 (2001).

67. Arriagada, C., Cobbold, P. R. & Roperch, P. Salar de Atacama basin: A record of compressional tectonics in the central Andes since the mid-Cretaceous. *Tectonics* **25** (2006).

68. Oncken, O. *et al.* in *The Andes. Frontiers in Earth Sciences* (eds Oncken, O. *et al.*) 3–27 (Springer, Berlin, Heidelberg, 2006).

69. Charrier, R., Pinto, L. & Rodríguez, M. in *The Geology of Chile* (eds Moreno, T. & Gibbons, W.) 21–114 (Geological Society of London, 2007).

70. Carrera, N., Muñoz, J. A., Sabat, F., Mon, R. & Roca, E. The role of inversion tectonics in the structure of the Cordillera Oriental (NW Argentinean Andes). *Journal of Structural Geology* **28,** 1921–1932 (2006).

71. Coira, B., Davidson, J., Mpodozis, C. & Ramos, V. Tectonic and Magmatic Evolution of the Andes of Northern Argentina and Chile. *Earth-Science Reviews* **18,** 303–332 (1982).

72. Horton, B. K. Tectonic Regimes of the Central and Southern Andes: Responses to Variations in Plate Coupling During Subduction. *Tectonics* **37,** 402–429 (2018).

73. Maloney, K. T., Clarke, G. L., Klepeis, K. A. & Quevedo, L. The Late Jurassic to present evolution of the Andean margin: Drivers and the geological record. *Tectonics* **32,** 1049–1065 (2013).

74. Armijo, R., Lacassin, R., Coudurier-Curveur, A. & Carrizo, D. Coupled tectonic evolution of Andean orogeny and global climate. *Earth-Science Reviews* **143,** 1–35 (2015).

75. Schellart, W. P., Freeman, J., Stegman, D. R., Moresi, L. & May, D. Evolution and diversity of subduction zones controlled by slab width. *Nature* **446,** 308–311 (2007).

76. Schellart, W. P. Overriding plate shortening and extension above subduction zones: A parametric study to explain formation of the Andes Mountains. *Geological Society of America Bulletin* **120,** 1441–1454 (2008).

77. Assumpcao, M., Feng, M., Tassara, A. & Julia, J. Models of crustal thickness for South America from seismic refraction, receiver functions and surface wave tomography. **609.** Tectonophysics, 82–96 (2013).

78. Yuan, X., Sobolev, S. V. & Kind, R. Moho topography in the central Andes and its geodynamic implications. *Earth and Planetary Science Letters* **199,** 389–402 (2002).

79. Burbank, D., Meigs, A. & Brozovic, N. Interactions of growing folds and coeval depositional systems. *Basin Research* **8,** 199–223 (1996).

80. Burbank, D. W., McLean, J. K., Bullen, M., Abdrakhmatov, K. Y. & Miller, M. M. Partitioning of intermontane basins by thrust-related folding, Tien Shan, Kyrgyzstan. *Basin Research* **11,** 75–92 (1999).

81. Humphrey, N. F. & Konrad, S. K. River incision or diversion in response to bedrock uplift. *Geology* **28,** 43–46 (2000).

82. Van der Beek, P., Champel, B. & Mugnier, J. L. Control of detachment dip on drainage development in regions of active fault-propagation folding. *Geology* **30,** 471–474 (2002).

83. Tomkin, J. H. & Braun, J. Simple models of drainage reorganisation on a tectonically active ridge system. *New Zealand Journal of Geology and Geophysics* **42,** 1–10 (1999).

84. Baldwin, J. A., Whipple, K. X. & Tucker, G. E. Implications of the shear stress river incision model for the timescale of postorogenic decay of topography. *Journal of Geophysical Research-Solid Earth* **108** (2003).

85. Burov, E. & Diament, M. Isostasy, equivalent elastic thickness, and inelastic rheology of continents and oceans. **24.** Geology, 419–422 (1996).

86. Watts, A. B. & Burov, E. B. Lithospheric strength and its relationship to the elastic and seismogenic layer thickness. **213.** Earth Planet Sc Lett, 113–131 (2003).